Acoustic Float Tracking with the Kalman Smoother

PAUL CHAMBERLAIN,[a] BRUCE CORNUELLE,[a] LYNNE D. TALLEY,[a] KEVIN SPEER,[b,c] CATHRINE HANCOCK,[b]
AND STEPHEN RISER[d]

[a] Scripps Institution of Oceanography, University of California, San Diego, San Diego, California
[b] Geophysical Fluid Dynamics Institute, Florida State University, Tallahassee, Florida
[c] Department of Scientific Computing, Florida State University, Tallahassee, Florida
[d] College of the Environment, University of Washington, Seattle, Washington

(Manuscript received 17 May 2021, in final form 23 June 2022)

ABSTRACT: Acoustically tracked subsurface floats provide insights into ocean complexity and were first deployed over 60 years ago. A standard tracking method uses a least squares algorithm to estimate float trajectories based on acoustic ranging from moored sound sources. However, infrequent or imperfect data challenge such estimates, and least squares algorithms are vulnerable to non-Gaussian errors. Acoustic tracking is currently the only feasible strategy for recovering float positions in the sea ice region, a focus of this study. Acoustic records recovered from underice floats frequently lack continuous sound source coverage. This is because environmental factors such as surface sound channels and rough sea ice attenuate acoustic signals, while operational considerations make polar sound sources expensive and difficult to deploy. Here we present a Kalman smoother approach that, by including some estimates of float behavior, extends tracking to situations with more challenging datasets. The Kalman smoother constructs dynamically constrained, error-minimized float tracks and variance ellipses using all possible position data. This algorithm outperforms the least squares approach and a Kalman filter in numerical experiments. The Kalman smoother is applied to previously tracked floats from the southeast Pacific (DIMES experiment), and the results are compared with existing trajectories constructed using the least squares algorithm. The Kalman smoother is also used to reconstruct the trajectories of a set of previously untracked, acoustically enabled Argo floats in the Weddell Sea.

KEYWORDS: Ocean; Antarctica; Sea ice; Acoustic measurements/effects; In situ oceanic observations; Profilers, oceanic

1. Introduction

From their introduction, autonomous, acoustically tracked instruments have explored poorly sampled ocean areas and provided fundamental insight into ocean dynamics (Gould 2005). First deployed in 1955 (Swallow 1955), autonomous float endurance has improved from days to years and now represents a mature technology (Rossby et al. 1986; Roemmich et al. 2019). Thousands of acoustically tracked floats have been deployed in most of the world's oceans at depths ranging from just below the surface to 4000 m (Ramsey et al. 2018). Acoustically tracked floats are typically localized at 6-h to daily intervals and have relatively high temporal resolution compared to mesoscale circulation. Lagrangian observations have been used to study mesoscale eddies, infer large-scale circulation (Boebel et al. 1997), and investigate stirring (Gille et al. 2007) and abyssal circulation (Hogg and Owens 1999).

Modern acoustic float instrumentation and methodology, developed by Rossby et al. (1986), is called RAFOS and consists of an acoustic receiver on each float. An array of moored sound sources (see Figs. 1–3) transmits sound at staggered intervals. Sound pulses received and recorded by a float are used to calculate a range from the float to the sound source. The float can be localized if multiple sound pulses are heard (ideally three or more) (Figs. 2, 3). Unstable or unusable trajectories can result if sufficiently precise ranging observations are not available. The publicly available ARTOA software package has automated this localization process with a least squares algorithm (Wooding et al. 2005; WHOI 2017). All sound sources broadcast at the same frequency, and this ambiguity can confound float tracking, as noted by Hogg and Owens (1999). The ARTOA algorithm makes no predictive estimate of float location; hence, it can be difficult to distinguish likely sound sources.

Autonomous floats can be particularly useful in sea ice–covered polar regions with substantial seasonal cycles (Gray et al. 2018). Polar regions are important for water mass transformation, subduction of heat and carbon, and ventilation of nutrients (Sarmiento et al. 2004). Polar regions are difficult to navigate; consequently, shipboard data coverage is poor and seasonally biased toward the warmer summer months (Riser et al. 2016). Argo floats are a tool for studying ocean structure and processes on many spatial and temporal scales (Riser et al. 2016; Johnson et al. 2022). With the advent of increasingly miniaturized sensors, Argo floats are now collecting data relevant to biogeochemistry and mixing (Johnson and Claustre 2016; Roemmich et al. 2019). The Weddell Sea has been observed with numerous autonomous drifting Argo floats that profile to the sea surface every 10 days, operating with sea ice avoidance software (Klatt et al. 2007; Reeve et al. 2016; Campbell et al. 2019). However, such polar observations are still challenging due to environmental factors (Abrahamsen 2014). Argo floats that happen to journey underneath the ice may spend more than a year unable to acquire position data. The geographical context of geophysical observations is

---

Corresponding author: Paul Chamberlain, pchamber@ucsd.edu

DOI: 10.1175/JTECH-D-21-0063.1

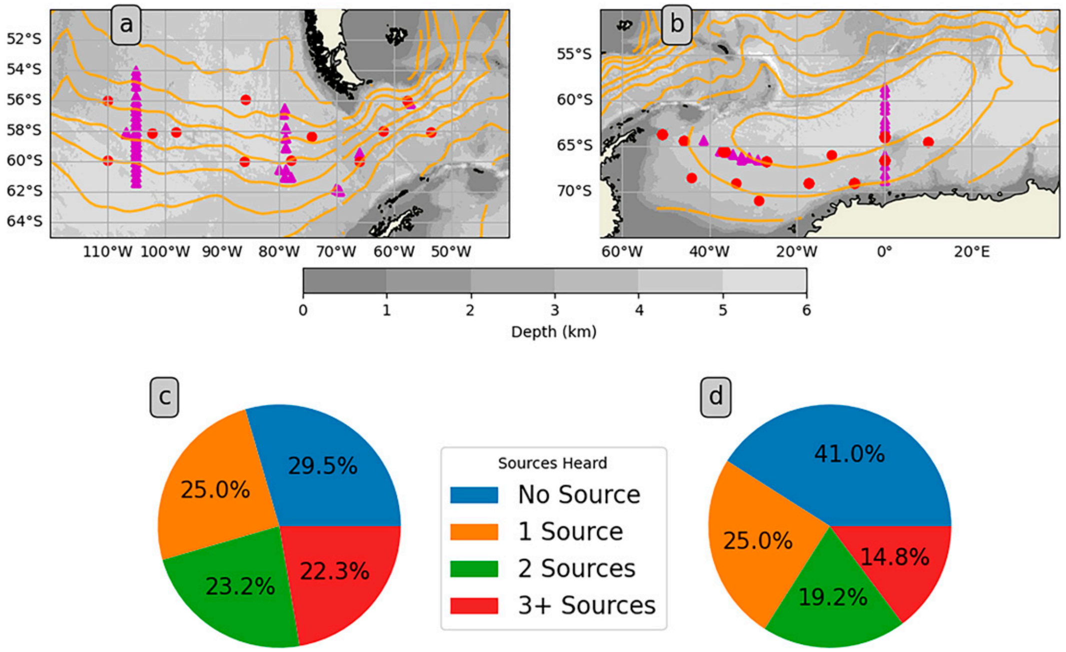

FIG. 1. (top) Bathymetry (gray shading) and sound source locations (red dots) for the (a) Drake Passage and (b) Weddell Sea. Magenta triangles indicate float deployment locations and orange lines indicate geostrophic streamlines at 1000 m depth contoured at 15 $m^2\ s^{-2}$ intervals (Gray and Riser 2014). (bottom) Distribution of the number of sources heard in the acoustic record for the (c) DIMES experiment and the (d) Weddell Sea, respectively.

important for understanding their true significance, but position uncertainty grows with the duration of position loss (Chamberlain et al. 2018; Yamazaki et al. 2020; Wallace et al. 2020; Nguyen et al. 2020). Float trajectories can also infer important ocean dynamics. These dynamics are resolved at a scale of motion related to both the density of float trajectories and the fidelity to which the true float trajectories are resolved from observations.

Acoustic tracking is, currently, the only technology for estimating float position under sea ice. In addition to nonprofiling RAFOS-type floats, some Argo floats in the Weddell Sea have been outfitted with acoustic RAFOS receivers to allow underice tracking (Klatt et al. 2007). However, the polar latitudes are environmentally challenging for straightforward acoustic tracking. Temperature decreases toward the surface in ice-covered seas; thus, sound is refracted to the surface—a region where surface scattering from waves and jagged ice-bottom formations dramatically attenuate acoustic signals (Klatt et al. 2007). Additionally, logistical and operational realities make acoustic sound sources difficult and expensive to deploy. Consequently, the acoustic data records recovered in these regions may be noisy or incomplete; this makes tracking difficult.

In addition to acoustic ranging, satellite positioning, dynamical knowledge of the circulation, and past float velocities can also be used to constrain float trajectories. As a step beyond the established least squares acoustic tracking method, ARTOA (Wooding et al. 2005; WHOI 2017), we present a Kalman smoothing algorithm for float tracking that can work with more fragmented acoustic data by incorporating additional information and constraints. The Kalman smoother presented here is an innovation over ARTOA in that it uses simple kinematics to make predictions of the future system state and error covariances. ARTOA assumes persistence of the system state and does not predict error covariances. The Kalman smoother performs this calculation in both forward and reverse time, which applies an additional constraint on the trajectories over ARTOA calculations which are done in forward time only. Using variants of Kalman filters for vehicle or contact tracking is not new and is common for autonomous underwater vehicle localization (Kimball and Rock 2011; Webster et al. 2015), but to our knowledge, has never been applied to acoustically tracked oceanographic floats.

The Kalman filter generates sequential predictions of a float trajectory using kinematics (also known as the forecast). The prediction made in the forecast is shown as the orange × in Fig. 2. The Kalman filter then updates this prediction with positioning data when available; this update step is also known as the analysis and is shown as the green × in Fig. 2. During this analysis, new data can be checked against the predicted position (Fig. 2). Data that are highly improbable based on physical constraints and estimated uncertainties can be flagged or discarded, reducing the ambiguity of acoustic sources that broadcast with the same frequency. In the construction of the Kalman filter, we perform what is called a regularization on the trajectory solution by imposing several dynamical constraints to varying degrees. These include restricting the maximum float displacement, float velocity, and float velocity uncertainty. Float displacement was also minimized by imposing a tendency for

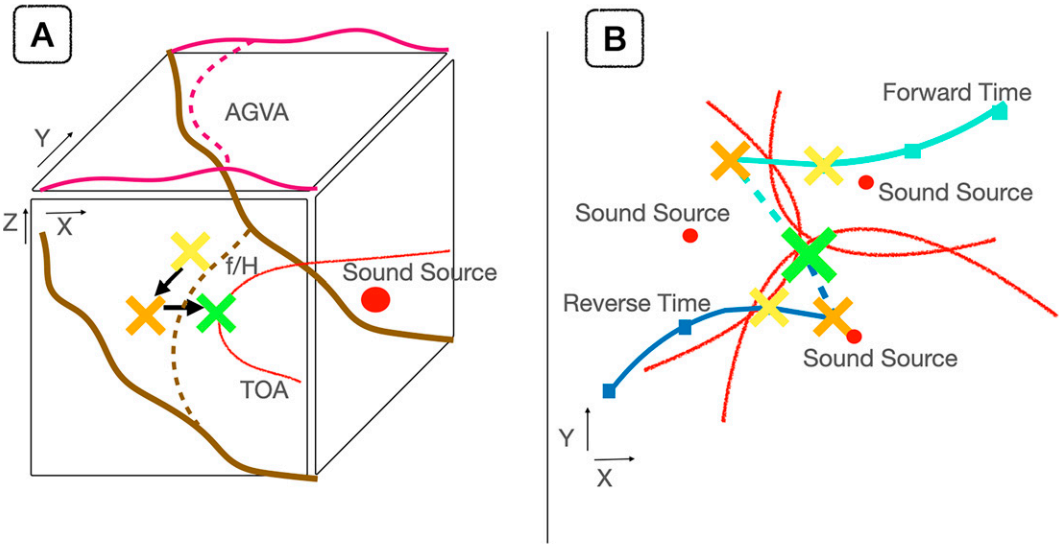

FIG. 2. Cartoon of Kalman smoother acoustic tracking scheme. Red dots represent sound source locations. Red arcs represent lines of position from ranging data observed on the float. (a) Dashed brown contour represents *f*/*H* field; dashed magenta contour represents geostrophic streamlines "AGVA" (Gray and Riser 2014). Yellow × represents previous position. Orange × represents the forecast. Green × represents the analysis all in forward time. (b) Light blue and dark blue squares represent Kalman filter derived positions in forward and reverse time, respectively. Yellow × symbols represents previous position in both forward and reverse time. Orange × symbols represent the Kalman filter analysis in both forward and reverse time. Dashed light blue and dark blue lines represent position updates due to smoothing routine. Green × represents Kalman smoother position estimate.

the float trajectory to relax to a linearly interpolated position between satellite positions, as shown in Wong and Riser (2011). We implement dynamical regularization by including a tendency term for float trajectories to follow barotropic planetary geostrophic streamlines (LaCasce 2000; Reeve et al. 2016; Chamberlain et al. 2018; Yamazaki et al. 2020) and geostrophic streamlines calculated from objectively mapped Argo-based dynamic height and velocity (Gray and Riser 2014).

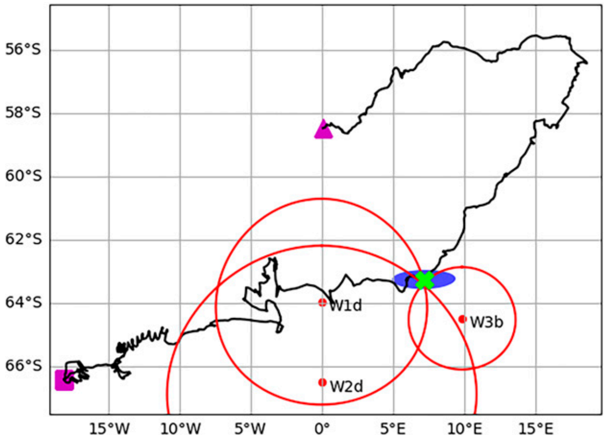

FIG. 3. Example of acoustic tracking from float 5901718 in the Weddell Sea. Green cross represents the most likely float position. Magenta triangle and square represent float start and end points, respectively. Black line represents the reconstructed float trajectory. Teal ellipse represents the position uncertainty ellipse at the 95% confidence interval (1.96 standard deviations). Red dots and lines represent locations and estimated time fronts for sound sources W1d, W2d, and W3b.

When a float emerges from under sea ice, it communicates its acoustic ranging data so that the floats underice trajectory can be estimated. The last satellite-derived position before the float went under the ice and the first satellite position when the float emerges from the ice are both strong constraints on its trajectory. Using the last satellite position before the float went under ice, and working in forward time, we can estimate the float's trajectory with available acoustic ranging. The forward prediction is shown as the orange × along the light blue track in Fig. 2. Similarly, a different estimate of the float's trajectory is produced using the first satellite position after the float emerged from the ice and working backward in time. The reverse time estimate is shown as the orange × along the dark blue track in Fig. 2. A Kalman smoother combines these forward and reverse time trajectory estimates to create an error-minimized estimate of position (green × in Fig. 2).

Here we present a new method based on Kalman smoothing that extends the useful data, allowing consistent acoustic float tracking when acoustic signals are of lower quality, and incorporating surface GPS positioning when available. This method can also incorporate additional external constraints, such as satellite altimetry and the influence of bathymetry, on the currents that advect the floats. In section 2, we describe the acoustically tracked float datasets, the basics of acoustic tracking, and the datasets used as external constraints. In section 3, we describe the synthetic dataset used to test the

Kalman smoother approach. In section 4, we present the new Kalman smoother approach for locating acoustically enabled floats. We then quantify the Kalman smoother performance using the particle simulation experiments (section 5a) and compare the Kalman smoother float track solutions to a previously tracked (using ARTOA) set of floats deployed in the Drake Passage during the DIMES experiment (Gille et al. 2007; Balwada et al. 2016) (section 5b). Finally, with insight gained from this, solutions are presented for a previously untracked set of acoustically enabled Argo floats deployed in the Weddell Sea (section 5c).

2. Data

For the application and testing of our Kalman smoother method for tracking acoustic floats, we use two separate acoustic float datasets from the Southern Ocean and a numerical simulation of acoustically tracked floats (next section). One of the acoustic datasets is derived from acoustically enabled Argo floats, so we first describe Argo profiling floats and then the acoustic tracking. Finally, we describe the DIMES and Weddell Sea experiment floats and ancillary datasets.

a. Core Argo

Argo profiling floats now comprise a global sustained observing system of about 4000 floats (Roemmich et al. 2019), and are the most widely used deep-ocean floats. Argo floats drift at about 1000 m and then profile from 2000 m to the sea surface. Satellites are used to track Argo floats when they surface (only a few experiments have used acoustically enabled Argo floats). Argo floats attempt to surface when they profile nominally every 10 days. However, Argo floats in sea ice regions, such as the Weddell Sea floats presented here, may not be able to surface when they profile, and the observations they collect while underice will not have a satellite-derived position. These underice profiles are commonly assigned a position based on a linear interpolation between the satellite-derived positions at the beginning and end of the sea ice season; the resulting position errors under the ice can reach 100–200 km (Chamberlain et al. 2018; Yamazaki et al. 2020). While Argo float observations are motivated mainly by temperature, salinity, and other properties measured during the vertical profiling (Roemmich et al. 2019), the 10-day positions are of great value for deep ocean circulation studies (Katsumata and Yoshinari 2010; Gray and Riser 2014; Ollitrault and Colin de Verdière 2014).

b. Acoustically tracked floats

Floats with the modern RAFOS-type receiver (Rossby et al. 1986) are localized much more frequently than the 10-day intervals of Argo profiling floats. Standard RAFOS floats are ballasted to remain at a single drift pressure after deployment. These floats surface only at the end of their mission to report a final position and relay the acoustic-ranging data they have collected throughout their mission. Daily or more frequent positions provide information about the velocity field not represented in the 10-day positions of Argo floats. Argo profiling floats can also be equipped with RAFOS receivers (RAFOS-enabled Argo floats). Like Argo profiling floats, RAFOS-enabled Argo floats provide full 2000-m temperature and salinity profile every 10 days. However, they have the advantage of being much more frequently tracked while they drift (nominally) at 1000 m than the standard Argo float.

Acoustically tracked floats require an array of sound sources, optimally at least three sources, within range of each float tracked float; however, two acoustic ranges combined with a prior position can typically position a float. Figure 3 shows an example of typical acoustic ranging. Each acoustic source in the regional arrays described here is programmed to broadcast at staggered times every day. As all sources broadcast the same tone, the identity of each received transmission is deduced by recognizing the operational limit of the broadcast range [≈300–700 km within sea ice (Klatt et al. 2007) and 1000 km or greater in the open ocean (Hogg and Owens 1999)] and finding local sources in this broadcast window that could be responsible. Skilled operators do sound source identification, but sound sources can be ambiguous and misidentifications are a fundamental nonlinearity in this workflow. Once the source is identified, the time of arrival (TOA) is calculated by subtracting the time the source transmitted sound from the time the float receives the signal.

Both float and source clocks are imperfect and drift over time. Due to the high speed of sound in seawater compared to the drift speed of instruments, these biases and uncertainties can result in substantial positioning errors if left uncorrected. Float clocks may be calibrated against satellite clocks while at the surface. During extended periods under the ice, floats cannot recalibrate clocks, and errors can become substantial. Upon deployment and recovery, acoustic source clock times are checked against ship-based clocks, and their offsets are measured. If sources cannot be recovered, their final clock offsets are unknown.

In our analysis, all measured source clock offsets were linearly interpolated from the time of source deployment to recovery; linearly interpolated sound source clock drift is then used to correct the TOA record of any floats positioned from a given sound source. Sound source clock linear interpolation introduces uncertainty, which is included in the parameterized TOA noise discussed in section 4. TOA can be transformed to distance if the sound speed of the medium is known. We assume sound signals travel along geodesics; however, refracted sound paths in the ocean have (one or more) arc lengths that are farther than the geodesic distance—especially in the ice-covered ocean (Spiesecke 2018). Errors in timing translate to errors in acoustic ranging distance; the error in the positioning fix based on the errors in ranging distance depends on the sound sources' geometry. A straightforward strategy for reducing error due to increased path length is to lower the speed of sound to account for the slower distance over ground that bending sound paths take. Our analysis did not account for the potential of multipath sound detections (the process through which one sound transmission can take two or more paths to get to a receiver and be recorded). This is a fundamental gap in our analysis.

TABLE 1. WMO ID numbers of 22 previously untracked Weddell Sea floats.

RAFOS enabled Argo floats			
5901716	5901717	5901718	5901720
5901721	5901723	5901724	5901727
5901728	5901730	5901731	5901733
5901734	5901735	5901737	5901738
5901739	5901740	5901741	5901742
5901743	5901744		

c. *DIMES floats*

The first of two acoustically tracked datasets we examine is from the DIMES experiment (Gille et al. 2007), in which 138 neutrally buoyant RAFOS floats were deployed west of Drake Passage. The first floats were deployed in January 2009; the last float surfaced in March 2012. Twelve different sound sources tracked the floats deployed west of and within Drake Passage (Fig. 1). In total 142 015 TOA observations were made by the DIMES floats throughout the experiment. DIMES trajectories were estimated from these TOAs (Balwada et al. 2016) using the least squares ARTOA tracking method (Wooding et al. 2005; WHOI 2017), and have been used in studies of mixing and dynamics of this region (LaCasce et al. 2014; Balwada et al. 2016, 2021). These ARTOA-based trajectories are deemed robust because the number and location of sound sources were sufficient.

d. *Weddell Sea floats*

Our second (and primary) dataset, which prompted the development of the Kalman smoother approach for estimating trajectories (Chamberlain et al. 2018), is a set of 22 acoustically enabled Argo floats deployed in the Weddell Sea from February 2008 to February 2013 (Fig. 1; Table 1). During this period, an array of 14 sound sources maintained by the Alfred Wegener Institute was available for multiyear float tracking (Fahrbach et al. 2011). Argo floats profile every 10 days and, unless prevented by sea ice, surface and broadcast their data. Argo floats also record a satellite-derived position when at the surface. The 10-day temperature and salinity profiles were disseminated as part of the operational global Argo dataset, with satellite positions when the floats surfaced and linearly interpolated positions when the floats were under sea ice.

These 22 Weddell Sea floats were acoustically enabled to allowing tracking through the winter. However, sea ice and local stratification degrade the acoustic range in the Weddell Sea (Klatt et al. 2007); this degradation resulted in difficulties with the standard ARTOA method for tracking the floats despite the large number of sound sources. To improve the tracking, the Kalman smoother was applied, and the resulting float trajectories were used in Chamberlain et al. (2018) to estimate position uncertainty arising from the lack of satellite fixes for the 10-day Argo profiles during the sea ice season. The Weddell Sea acoustically enabled Argo float dataset includes 13 966 TOA measurements and 1263 GPS satellite positions. GPS position data were downloaded from the USGODAE Argo GPS GDAC Data Browser (Argo 2019).

e. *Ancillary data*

For our Kalman smoother solution (section 4), we used two dynamical constraints: a tendency to follow (i) barotropic planetary geostrophic streamlines (LaCasce 2000; Reeve et al. 2016; Chamberlain et al. 2018; Yamazaki et al. 2020), and (ii) geostrophic streamlines calculated from objectively mapped Argo-based dynamic height and velocity (Gray and Riser 2014). The mathematical shorthand of fH^{-1} will refer to Barotropic planetary geostrophic streamlines, where f is the Coriolis parameter, and H is the water depth; geostrophic streamlines will refer to the Gray and Riser (2014) product. We used the "ETOPO1" 1 Arc-Minute Global Relief Model (Amante and Eakins 2009) for H in the fH^{-1} contours. A Gaussian filter with a standard deviation of 4 arc min was applied to the bathymetry dataset to reduce high-wavenumber variability through convolution with a Gaussian function. This relatively aggressive smoothing was necessary to make it possible to calculate a meaningful gradient.

3. Numerical particle tracking experiment

In addition to comparing the DIMES float trajectories calculated using the Kalman smoother with those from the ARTOA method, we compare these tracking schemes using a series of numerical particle tracking experiments. In the ocean, the true trajectory of a float is unknown, but we designed artificial experiments where true particle position and velocity statistics is known. The artificial experiments quantified the relative performance of the least squares, Kalman, and Kalman smoother filters in various observational uncertainty and float motion scenarios.

Our numerical experiments simulated float motion in the Weddell Sea by seeding numerical particles into the ocean and tracking them with each of the filters presented. Particles experienced horizontal advection at a depth of 1000 m and did not profile up and down; these numerical particles were intended to simulate float behavior. The numerical experiments used 30 000 particles to generate performance metrics over a wide range of positioning and instrument noise scenarios. Each particle had a unique trajectory and an observational dataset with distinct observation noise and observational density. The particles all had a starting location of 64°S, 23.5°W and were advected forward for 100 days in a semirandom horizontal flow. A hybrid Brownian motion model was used to simulate particle advection; a simple stochastic differential equation estimated daily particle velocity:

$$V(t) = V(t)_{\text{mean}} + sW(t), \qquad (1)$$

where $V(t)_{\text{mean}}$ is a mean velocity that we chose to have the same amplitude as the standard deviation of the Weddell Sea Argo velocity data (7.4 km day^{-1} zonal velocity and 5.3 km day^{-1} meridional velocity); $W(t)$ is a normally distributed random increment with an amplitude equal to the standard deviation of the Weddell Sea Argo array velocities; and s is a

TABLE 2. Sequential calculations of Kalman smoother algorithm.

Forward filter	
Initialization	$\mathbf{x}^a(t_0) = \boldsymbol{\mu}_0$ with error covariance $\mathbf{P}^a(t_0)$
Model forecast step/predictor [Eq. (6)]	$\mathbf{x}^f(t_i) = M_{i-1}\mathbf{x}^a(t_{i-1})$
	$\mathbf{P}^f(t_i) = M_{i-1}\mathbf{P}^a(t_{i-1})M_{i-1}^{\mathrm{T}} + \mathbf{Q}(t_{i-1})$
Data assimilation step/corrector [Eqs. (10)–(12)]	$\mathbf{d}_i = \mathbf{y}_i^o - \mathbf{H}_i \cdot \mathbf{x}^f(t_i)$
	$\mathbf{K}(t_i) = \mathbf{P}^f(t_i)\mathbf{H}_i^{\mathrm{T}}[\mathbf{H}_i\mathbf{P}^f(t_i)\mathbf{H}_i^{\mathrm{T}} + \mathbf{R}_i]^{-1}$
	$\mathbf{P}^a(t_i) = [\mathbf{I} - \mathbf{K}(t_i)\mathbf{H}_i]\mathbf{P}^f(t_i)$
	$\mathbf{x}^a(t_i) = \mathbf{x}^f(t_i) + \mathbf{K}(t_i)\mathbf{d}_i(t_i)$
Smoother	
Initialization	$\mathbf{x}^s(t_N) = \mathbf{x}^a(t_N)$
	$\mathbf{P}^s(T_N) = \mathbf{P}^a(T_N)$
Update	$\mathbf{K}^s(t_i) = \mathbf{P}^a(t_i)M_i^{\mathrm{T}}[\mathbf{P}^f(t_{i+1})^{-1}]$
	$\mathbf{P}^s(t_i) = \mathbf{P}^a(t_i) - \mathbf{K}^s(t_i)\mathbf{P}^s[t_{i+1} - \mathbf{P}^f(t_{i+1})][\mathbf{K}^s(t_i)]^{\mathrm{T}}$
	$\mathbf{x}^s(t_i) = \mathbf{x}^a(t_i) + \mathbf{K}^s(t_i)[\mathbf{x}^s(t_{i+1}) - \mathbf{x}^f(t_{i+1})]$
Regularizations	
Max velocity uncertainty	60 km day^{-1}
Max velocity	35 km day^{-1}
Max displacement	50 km

scalar that is varied to test the effects of signal (mean flow) to noise (random increment) ratio in this simple example of particle flow. We report experiments with s values of 0.1, 0.3, and 0.7, and equally divide the particles between these advection states. Larger values of s were experimentally calculated, but the performance of each seemed to saturate above s values of 0.7. The simulated sound source array consisted of six sources uniformly distributed within a 600 km radius of the starting position.

One of the goals of the numerical float experiment is to assess the variables that control the position estimate errors. A distinct TOA noise amplitude, number of sound sources heard, and chance of satellite positioning was randomly assigned to each of the 30 000 particles upon initialization. TOA noise amplitude was uniformly distributed between 1 and 50 s; the number of sound sources heard was uniformly distributed between 1 and 6; and the chance of satellite positioning was uniformly distributed between 0% and 100%.

At every time step in each particle's trajectory, a number of TOA observations equal to the sound source number was generated for the particle; each TOA observation was randomly assigned to be transmitted from a source within the array with uniform distribution. The true distance from each sound source to the particle was known, and the acoustic travel time was calculated using this distance and a speed of sound of 1.5 km s^{-1}. This true TOA was then degraded by adding a normally distributed term with an amplitude equal to the TOA noise amplitude. At every time step, these "noisy" TOA were then used to test each filter's performance in reconstructing the true trajectory. In addition to acoustic tracking, RAFOS-enabled Argo floats also receive satellite positioning; to assess the impact of intermittent satellite observations, we included satellite positioning with uniform probability equal to the chance of satellite positioning at each daily time step.

4. Methods

The Kalman filter literature is ample and mature (Wunsch 2006; Rauch et al. 1965) so the following is a brief recapitulation in the notation of Ide et al. (1997) and is described sequentially in Table 2: specifically, the subscript i denotes the time step, boldface lowercase variables denote vectors, boldface sans serif uppercase letters denote matrices, and italic uppercase letters denote nonlinear processes.

For the reader's convenience, this section (and the associated table) is broken into the following subsections: Kalman forward filter, Kalman smoother, regularizations, and processing techniques. A flowchart (Fig. 4) also provides an overview of these calculations.

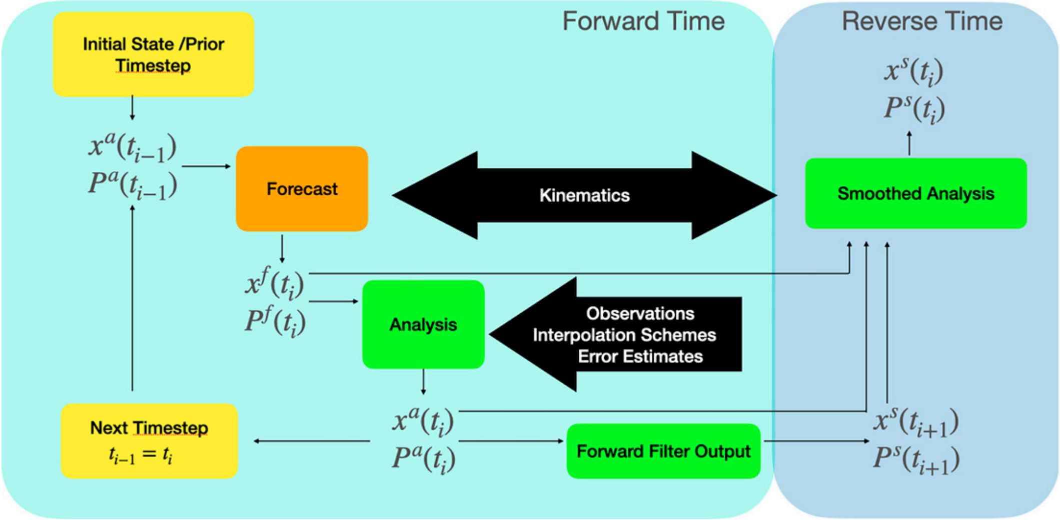

FIG. 4. Flowchart describing the Kalman smoother calculation. Light blue shading represents calculations in forward time; dark blue shading represents calculations in reverse time. Yellow boxes represent initial time steps, orange boxes represent the forecast, and green boxes represent the analysis.

a. *Kalman forward filter*

Kalman filtering is a sequential least squares linear estimator that assumes all observations have zero mean with normal distribution. In words, the Kalman filter starts with an estimate of the state of the system which we call the analysis (yellow box in Fig. 4), and uses a model to create a predicted state which we call the forecast (orange box in Fig. 4), then compares the predicted state to observations to create a new analysis (green box in Fig. 4), and finally uses the analysis as the initial state to create the forecast in the next time step. This process of sequentially propagating the analysis forward to create a forecast and then updating the forecast with new observations can continue as long as there are new observations to assimilate. The superscripts a and f denote the analysis and forecast, respectively. The superscript t denotes true state vectors, and the superscript T denotes transposes.

We begin with the position and velocity of the previous time step ($i-1$), which we call the true state vector $\mathbf{x}^t(t_{i-1})$. The true state vector is propagated to the next time step with a simple kinematic transition matrix with a frictional term such that

$$\mathbf{x}^t(t_i) = M_{i-1}\mathbf{x}^t(t_{i-1}) + \boldsymbol{\eta}_{i-1}, \tag{2}$$

where $\boldsymbol{\eta}$ is the model noise process, which is the error of the model M_{i-1}, which we assume to have a zero-mean normal distribution that is stationary over time. The covariance $\mathbf{Q}$ of the model noise process is written:

$$\mathbf{Q} = E[\boldsymbol{\eta}_{i-1}\boldsymbol{\eta}_{i-1}^{\mathrm{T}}], \tag{3}$$

where E is the expectation operator. Process noise ($\mathbf{Q}$) will generally be used to describe both process position noise and process velocity noise. Process noise is the effect of unmodeled velocities and accelerations caused by forcing (such as ocean variability) not accounted for in the simple kinematics. The deterministic component of Eq. (2), M_{i-1}, is written using $\mathbf{z}$ for the horizontal location of the float:

$$\begin{cases} \mathbf{x}(t_i) = \begin{bmatrix} \mathbf{z}(t_i) \\ \dot{\mathbf{z}}(t_i) \end{bmatrix}, \\ \mathbf{z}(t_i) = \mathbf{z}(t_{i-1}) + \Delta t\dot{\mathbf{z}}(t_{i-1}), \\ \dot{\mathbf{z}}(t_i) = \alpha\dot{\mathbf{z}}(t_{i-1}), \end{cases} \tag{4}$$

where α is a frictional factor that we set to 0.95, Δt is the time step, $\mathbf{z}$ is the position component of $\mathbf{x}^t$, and $\dot{\mathbf{z}}$ is the velocity component of $\mathbf{x}^t$. The implementation of the Kalman filter presented here only includes float position and velocity. Acceleration is modeled as a white noise process [Eq. (2)].

We begin tracking with an estimate of the position and velocity from a prior time step [the analysis or $\mathbf{x}^a(t_{i-1})$] and an estimate of the analysis error covariance from the previous time step. The analysis error covariance is written as follows:

$$\mathbf{P}^a(t_{i-1}) = E[\{\mathbf{x}^t(t_{i-1}) - \mathbf{x}^a(t_{i-1})\}\{\mathbf{x}^t(t_{i-1}) - \mathbf{x}^a(t_{i-1})\}^{\mathrm{T}}]. \tag{5}$$

The analysis and the analysis error covariance are then predicted forward to the next time step by the kinematic model, including process noise:

$$\begin{aligned} \mathbf{x}^f(t_i) &= M_{i-1}\mathbf{x}^a(t_{i-1}), \\ \mathbf{P}^f(t_i) &= M_{i-1}\mathbf{P}^a(t_{i-1})M_{i-1}^{\mathrm{T}} + \mathbf{Q}(t_{i-1}). \end{aligned} \tag{6}$$

This is the forecast in Fig. 4 and is represented by the orange × in Fig. 2.

The next step is to use new observations to update the forecast using observations. Satellite-derived positions are linear, but other observations contain nonlinear terms in the calculation used to constrain position (e.g., magnitude of distance expressed as $\sqrt{\mathbf{r}_i \cdot \mathbf{r}_i^{\mathrm{T}}}$, where $\mathbf{r}_i$ is the vector from source to float position). As such, we use the extended Kalman filter formulation of the equations. The extended Kalman filter approximates the nonlinear terms with a first-order Taylor expansion, which may lead to unstable performance if the observation and state variables differ substantially. The linearized observation matrix transforms the state vector into observation space and in the nonlinear formulation is expressed as the Jacobian $H_i' = \mathbf{H}_i = d\mathbf{g}/d\mathbf{x}|_{x^f}$, where $\mathbf{g}$ is the nonlinear functional form of the observation expressed in terms of elements of the state vector. Specifically, the Jacobian elements for travel time are equal to

$$\mathbf{H}_i = \frac{r_i}{\sqrt{\mathbf{r}_i \cdot \mathbf{r}_i^{\mathrm{T}}} * c}, \tag{7}$$

where c is the sound speed, and the Jacobian elements for fH^{-1} contours and geostrophic streamlines are numerically derived. Observations are represented in the usual way as

$$\mathbf{y}_i^o = \mathbf{H}_i \cdot \mathbf{x}^t(t_i) + \boldsymbol{\epsilon}_i, \tag{8}$$

where $\mathbf{y}_i^o$ is the observation, $\mathbf{H}_i \cdot \mathbf{x}^t(t_i)$ is the true location transformed into observation space, and $\boldsymbol{\epsilon}$ is the observational noise process. Unlike the model noise process, we expect the observational noise process to change in time as we record a varying number of observations. The observation noise process is assumed to have a normal distribution and zero mean. We can write the covariance of the noise process as the following:

$$\mathbf{R}_i = E[\boldsymbol{\epsilon}_i \boldsymbol{\epsilon}_i^{\mathrm{T}}], \tag{9}$$

where $\mathbf{R}_i$ is the observation noise at time step i. The difference between this prediction from the actual observations is called the innovation and is written as

$$\mathbf{d}_i = \mathbf{y}_i^o - \mathbf{H}_i \cdot \mathbf{x}^f(t_i). \tag{10}$$

The new observations are used to update the forecast state (orange stars in Fig. 2) to the new analysis state by adding the innovation multiplied by a term known as the Kalman gain $\mathbf{K}$:

$$\begin{aligned} \mathbf{x}^a(t_i) &= \mathbf{x}^f(t_i) + \mathbf{K}(t_i)\mathbf{d}_i(t_i) \\ \mathbf{K}(t_i) &= \mathbf{P}^f(t_i)\mathbf{H}_i^{\mathrm{T}}[\mathbf{H}_i\mathbf{P}^f(t_i)\mathbf{H}_i^{\mathrm{T}} + \mathbf{R}_i]^{-1}, \end{aligned} \tag{11}$$

where $\mathbf{x}^a$ is the analysis state and is shown as the orange × in Fig. 2.

The Kalman gain is dependent on the relative magnitudes of the observation noise and the process noise. Suppose the observation noise is much smaller than the process noise (we trust the observations more than the kinematic forecast). In that case, the innovation (difference of observations from the forecast transformed into observation space) strongly influences the new analysis state. Alternatively, suppose the observation noise is much greater than the process noise (we trust the kinematic forecast more than the observations). In that case, the Kalman gain is close to zero, and the innovation does not influence the new analysis state. The analysis error covariance ($\mathbf{P}^a$) is proportional to the forecast error covariance ($\mathbf{P}^f$) multiplied by a correction term proportional to the identity matrix $\mathbf{I}$ minus the Kalman gain:

$$\mathbf{P}^a(t_i) = [\mathbf{I} - \mathbf{K}(t_i)\mathbf{H}_i]\mathbf{P}^f(t_i). \tag{12}$$

Consider the two limits to relative observation noise covariance ($\mathbf{R}$) versus process noise ($\mathbf{Q}$) in Eq. (12): suppose we trust the observations more than the kinematic forecast, then the Kalman gain ($\mathbf{K}$) is relatively large and the analysis error covariance ($\mathbf{P}^a$) is less than the kinematic model forecast error covariance ($\mathbf{P}^f$) (we gained new information from the observations and reduced position and velocity uncertainty); now suppose we trust the forecast more than the observations, then the Kalman gain ($\mathbf{K}$) is close to zero and the analysis error covariance ($\mathbf{P}^a$) will be of similar magnitude to the forecast error covariance ($\mathbf{P}^f$) (we gained little from the new observations and the position and velocity uncertainties remain the same). In the special case when there are no observations, the forecast error covariance ($\mathbf{P}^f$) will be increased by the prescribed process noise ($\mathbf{Q}$) every time step, and the analysis error covariance ($\mathbf{P}^a$) will equal the forecast error covariance ($\mathbf{P}^f$). Because process noise ($\mathbf{Q}$) is the unexpected acceleration due to unaccounted forcing, we can think of the increasing forecast error covariance ($\mathbf{P}^f$) as the growing summation of all of the unknown changes in the trajectory a float can take in the absence of ranging data. Equations (11) and (12) comprise the analysis step (Fig. 4). The analysis is then propagated forward in time via the forecast and updated with available observations in the analysis steps until new observations are exhausted (forward filter output in Fig. 4).

b. *Kalman smoother*

The Kalman filter is purely a forward calculation, meaning that time moves in only one direction and sequential information improves the state estimate. The forward Kalman filter is useful in applications where operational necessity prohibits collecting all observations before estimating the state, e.g., landing an airplane or tracking a missile. Floats cannot communicate with satellites while under ice, meaning that all acoustic ranging and depth data are communicated only after a float reaches open water or sea ice melts. As we will show, having all the observations available allows an additional constraint on the solution that reduces position error. The impact of these complete data is maximized here by using a variant of the Kalman filter called the Kalman smoother. Our application of the Kalman smoother estimates float tracks by creating trajectory estimates in both forward and reverse time, then combining the two in such a way as to minimize uncertainty (Fig. 2). Beginning with the analysis at the final time step of the forward Kalman filter, we have

$$\begin{aligned} \mathbf{x}^s(t_N) &= \mathbf{x}^a(t_N) \\ \mathbf{P}^s(T_N) &= \mathbf{P}^a(T_N) \end{aligned}, \tag{13}$$

where $\mathbf{x}^s(t_N)$ and $\mathbf{P}^s(t_N)$ are the smoothed estimates of the state vector and covariance matrix, respectively. Reproducing the error minimizing sequential calculation as the previous section, but in reverse time, leads to the following equations:

$$\begin{aligned}\mathbf{K}^s(t_i) &= \mathbf{P}^a(t_i)M_i^{\mathrm{T}}[\mathbf{P}^f(t_{i+1})]^{-1}\\ \mathbf{P}^s(t_i) &= \mathbf{P}^a(t_i) - \mathbf{K}^s(t_i)[\mathbf{P}^s(t_{i+1}) - \mathbf{P}^f(t_{i+1})]\mathbf{K}^s(t_i)^{\mathrm{T}}\,,\\ \mathbf{x}^s(t_i) &= \mathbf{x}^a(t_i) + \mathbf{K}^s(t_i)[\mathbf{x}^s(t_{i+1}) - \mathbf{x}^f(t_{i+1})]\end{aligned} \qquad (14)$$

where $\mathbf{K}^s$ is the smoothed Kalman gain. $\mathbf{x}^a(t_i)$ and $\mathbf{x}^f(t_{i+1})$ are orange × symbols along the dark and light blue tracks in Fig. 2, respectively. Equation (14) is the smoothed analysis (Fig. 4) and shown as the green × in Fig. 2.

c. Regularizations

To improve the stability and realism of our solution, we imposed several regularizations on the filter. Velocity uncertainty is restricted to be no greater than 60 km day^{-1}, maximum velocity is restricted to be no greater than 35 km day^{-1}, and the maximum daily change in position can be no more than 50 km. These velocity and position constraints are larger than the fastest velocity and position displacement recorded in the ARTOA-tracked DIMES solutions.

To improve the dynamics of the model and reduce ambiguities in the filter when there is an absence of ranging data, we imposed constraints that nudge the float to follow selected interpolation schemes. Linear interpolation between known satellite positions is referred to as satellite linear interpolation and is the simplest and first interpolation scheme suggested for underice data (Wong and Riser 2011). The uncertainty of this estimate has been studied (Chamberlain et al. 2018; Yamazaki et al. 2020), yielding mean uncertainty estimates of approximately 100 km for 6 months of position loss. The second scheme was a tendency for the float to follow fH^{-1} contours by nudging the current analysis such that the value of fH^{-1} was equal to that of the previous time step. A third scheme similarly nudged floats to follow geostrophic streamlines by updating the analysis such that the current geostrophic streamline value was equal to that of the previous time step. At each time step, these nudging terms were added via Eq. (10).

The code includes an optional check that helps flag spurious sound source identifications. This check compares the observed TOA anomaly (innovation) to the forecast error covariance and discards observations outside the 95% confidence interval of our forecast position. Removing these unlikely TOA observations helped mitigate sound source ambiguity (and the resultant nonlinearity of misidentification). ARTOA does not (and cannot) perform these checks.

d. Preprocessing

Preprocessing the acoustic data to remove sound source clock bias and drift was found to be important in reconstructing meaningful tracks. The DIMES float tracks are included in this analysis as a reference standard and, as such, are assumed to be correct. Any TOA difference between the calculated TOA (using the sound source to DIMES trajectory distance) and TOA in the acoustic record is considered TOA misfit. Misfit is defined as

$$\boldsymbol{\epsilon}_i^s = \mathbf{y}_i^o - \mathbf{H}_i \cdot \mathbf{x}^s(t_i). \qquad (15)$$

The Kalman smoother assumes that observational data are unbiased with a normal distribution of uncertainty; consequently, the mean TOA misfit and clock drift for each float was removed before running the Kalman smoother. TOA misfits greater than 35 s compared with the ARTOA DIMES trajectories were also deemed spurious and were excluded from our reconstructed float trajectories. Typically, ARTOA trajectories use a subset of available sound sources to produce float trajectories. For our calculations, all available sound source data were used. For the Weddell Sea floats, some satellite observations are available; we calculated a set of TOA based on the distance from the satellite-derived float position to the sources. We assume the difference between measured TOA and calculated TOA is caused by two sources of uncertainty: drift in the sound source clock and the regionally variable speed of sound. To correct these errors, a multiple linear regression was used to solve for optimal sound source clock drift and optimal sound speed. The multiple linear regression simultaneously calculated a sound source clock drift to minimize TOA misfit as a function of time since sound source deployment and a sound speed to minimize TOA misfit as a function of distance from float to sound source. The optimal correction to sound speed and clock drift was then used for all trajectory solutions.

e. Tuning experiment

One subtlety of our estimates is that they use the prescribed noise of various synthetic (fH^{-1} contours, geostrophic streamlines, satellite linear interpolation) and real (acoustic ranging, satellite positioning) observations as well as process noise to generate the final trajectory. The process noise and observation noise are variables $\mathbf{Q}$ and $\mathbf{R}$ in Eqs. (6) and (11), respectively. When the observations do not fully constrain the trajectory solution, the final trajectories can be sensitive to these choices.

To explore sensitivities to these prescribed uncertainties, we conducted an experiment that varied these parameters in what we considered to be extra small, small, medium, and large ranges. We explored the sensitivity of process position noise and process velocity noise in the $\mathbf{Q}$ matrix [Eq. (6)] and sensitivity to geostrophic streamline noise, fH^{-1} noise, and satellite linear interpolation noise (when GPS positions were available) in the observation noise [$\mathbf{R}$ of Eq. (11)]. Consequently, the total number of calculated runs scales as the fifth and sixth power (for DIMES and the Weddell Sea, respectively) of the number of values considered for each filter parameter. This is a computational burden.

Medium values were chosen to be either the variance of the observational dataset, or a dynamically reasonable value: specifically, 3 km for process position noise, 3 km day^{-1} for process velocity noise, 2.1×10^{-7} rad m^{-1}s^{-1} for fH^{-1} contour noise, and 20.0 m^2 s^{-1} for geostrophic streamline noise. The DIMES and Weddell Sea experiments (for which no trajectory solution has been published) used the same medium values. The Weddell Sea dataset also includes infrequent satellite

TABLE 3. Uncertainties considered for sensitivity experiments.

Parameter	XS (M/4)	S (M/2)	M	L (1.5 × M)	XL (2 × M)	XXL (2.5 × M)	XXXL (3 × M)
TOA (s)	2	4	8	12	16	20	24
Process position (km)	0.75	1.5	3	4.5			
Process velocity (km day^{-1})	0.75	1.5	3	4.5			
Satellite linear interpolation (km)			120				
Geostrophic streamline (m^2 s^{-1})	0.6×10^{-7}	1.1×10^{-7}	2.1×10^{-7}	3.2×10^{-7}			
fH^{-1} contour (rad m^{-1} s^{-1})	5	10	20	30			

positions, which vary by season and location within the gyre (Chamberlain et al. 2018). The medium noise value for satellite linear interpolation was 120 km. Extra small and small values were 25% and 50% of the medium value, respectively. Large values were 150% of the medium value.

Acoustic data misfit will be sensitive to the prescribed TOA noise. Because of this dependence, trajectory solutions were calculated for seven TOA noise conditions ranging from 2 to 24 s. The medium TOA noise value is defined as 8 s. Table 3 records all noise values used in these tuning experiments.

The data misfit [Eq. (15)] is sensitive to the values of process noise [**Q** in Eq. (6)] and observation noise [**R** in Eq. (11)]. The ideal filter tuning will have prescribed noise equal to the true uncertainty of the available positioning data and kinematic model skill. Adjusting the relative confidence in the forecast or the data may achieve lower TOA misfit (going to the limit of least squares when there is no confidence in either). However, it may not reproduce the true trajectories with fidelity. Reducing the prescribed TOA noise will cause the filter to more closely match TOA observations but may produce an overfit solution that adjusts too rapidly to noisy data. Conversely, too little confidence in the TOA data will result in an underfit solution that does not appropriately respond to real changes in the true float trajectory. To address these competing concerns, we introduce the following cost function (Ide et al. 1997; Parker 1994):

$$J = \sum_{i=0}^{n} (\boldsymbol{\epsilon}_i^s)^{\mathrm{T}} \mathbf{R}_0^{-1} \boldsymbol{\epsilon}_i^s + \sum_{i=0}^{n} [\mathbf{x}^s(t_i) - \mathbf{x}^f(t_i)]^{\mathrm{T}} \mathbf{P}_0^{-1} [\mathbf{x}^s(t_i) - \mathbf{x}^f(t_i)], \tag{16}$$

where $\mathbf{P}_0$ is an approximate background process noise covariance based on the medium values of position process noise and velocity process noise, and $\mathbf{R}_0$ is the observation noise covariance constructed from the medium TOA noise. The first term in Eq. (16) is a penalty on misfit between the data and the trajectory estimate and is called the data misfit. This term penalizes solutions that do not adequately adapt to data. The second term represents a penalty for smoothed solutions that update the forecast by a large amount relative to the prescribed process noise and is called the model norm. This term penalizes overfit solutions that may overcompensate the final trajectory based on noisy data. We

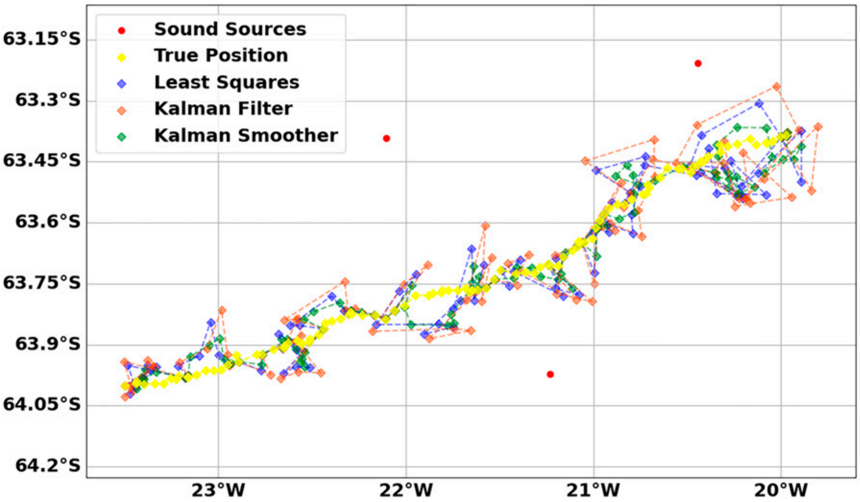

FIG. 5. Example trajectory reconstruction of particle release experiment. The true particle trajectory is represented by yellow diamonds with trajectories estimated from least squares (blue diamonds), Kalman filter (light red diamonds), and Kalman smoother (green diamonds). Red circles represent sound source locations.

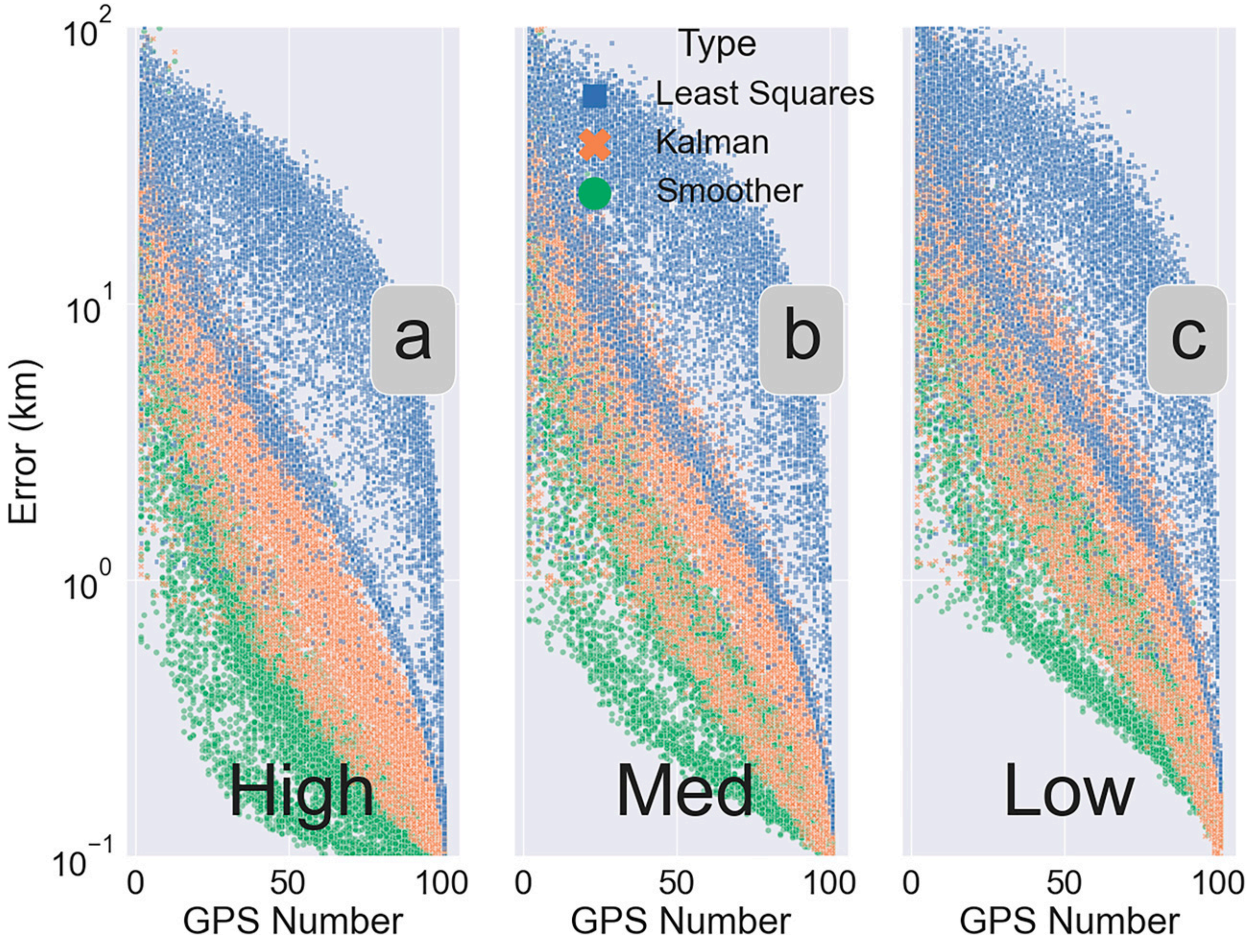

FIG. 6. Trajectory error for numerical simulation for Kalman smoother (green circle), Kalman filter (orange ×), and least squares (blue squares) algorithm for varying percentage of GPS positioning. The s value [Eq. (1)] is equal to (a) 10%—high signal-to-noise case; (b) 30%—medium signal-to-noise case; and (c) 70% of mean flow–low signal-to-noise case.

wish to minimize model norm and data misfit simultaneously. Only idealized multiparameter optimization problems have a single cost minimum, and the choice of metric that relates the model norm to the data misfit is a fundamental assumption. Thus we explore J by calculating many different solutions over the range of parameter values shown in Table 3. The curve defined by the lower bound of the calculated J in model norm–data misfit space is known as the Pareto frontier (Jahan et al. 2016). We choose to weight model norm and data misfit equally, and, consequently, the minimum of the second derivative of the Pareto frontier defines the location of the optimal solution.

In our calculations, we assume that satellite positioning uncertainty is well studied and comparably very accurate to all other forms of positioning discussed. These calculations used a satellite position uncertainty of 0.1 km, and considered no other values for satellite position uncertainty. We did not explore the parameter space of the numerical particle experiment because the true particle velocities and the uncertainty of the observations were previously known.

5. Results

We tested our method in three different scenarios:

1) We performed a numerical experiment with many examples of satellite positioning frequency and acoustic ranging data density and quality. These data tested the ability of the least squares (a method used by ARTOA), Kalman filter, and Kalman smoother algorithms to reconstruct the true trajectories.
2) We compared the Kalman smoother's performance against an ARTOA-tracked float dataset used in the DIMES experiment.
3) The Kalman smoother generated 22 trajectories for previously untracked floats in the Weddell Sea.

a. Particle release experiment

To generate additional confidence in the Kalman smoother and Kalman filter, and to compare their performance to other methods, we simulated the tracking of many numerically

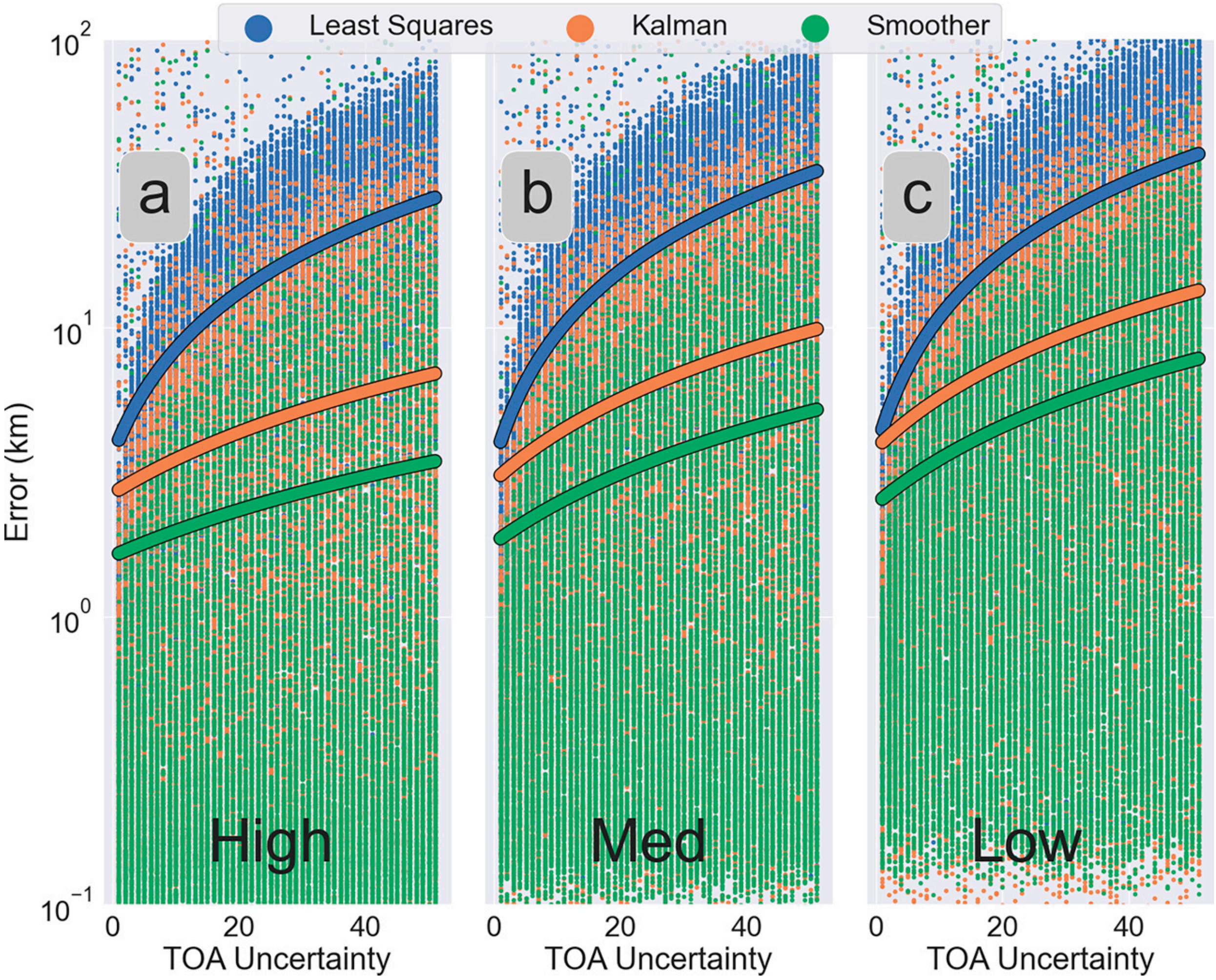

FIG. 7. Trajectory error for numerical simulation for Kalman smoother (green circle), Kalman filter (orange circle), and least squares (blue circle) algorithm for varying quality of acoustic positioning. Solid lines represent linear fit of available data. The *s* value [Eq. (1)] is equal to (a) 10%—high signal-to-noise case; (b) 30%—medium signal-to-noise case; and (c) 70% of mean flow–low signal-to-noise case.

generated particles seeded in the Weddell Sea (Fig. 5). All three filters considered in this analysis tracked particles. Simulated observations explored the observational parameter space by varying the number of satellite-derived positions available, the amount of acoustic tracking error, and the number of sound sources heard. The motion of the numerically generated particles was calculated with a simple stochastic differential equation [Eq. (1)], which decomposed the motion into a mean velocity component and a scaled normally distributed random component with amplitude proportional to the mean velocity. The skill of both the Kalman filter and the Kalman smoother is related to the predictive skill of the kinematics used to create the forecast [*M* in Eq. (6)]. The least squares filter as formulated uses persistence as the kinematic model [i.e., $\mathbf{z}(t_i) = \mathbf{z}(t_{i-1})$ and $\dot{\mathbf{z}}(t_i) = \dot{\mathbf{z}}(t_{i-1})$] for the forecast. Although this is mathematically a least squares solution, it only approximates the routine used by ARTOA. ARTOA includes a variety of other corrections that were not included in this calculation; however, we assume that this approximation is similar enough to be considered the null hypothesis for our tracking filter intercomparison.

One of the hypotheses of this particle release experiment was that the performance of the Kalman filter and Kalman smoother would degrade relative to the least squares filter as the motion of the particles became more random. This is because increasingly random particles reduce the kinematic model's predictive skill [*M* in Eq. (6)] compared to persistence. Eventually, as the kinetic model loses all skill, the performance of the Kalman filter and Kalman smoother should converge to the least squares solution. Additionally, because our formulation of the least squares solution makes no forecast, we expect the least squares trajectory error to be insensitive to the character of the float motion. To assess this, we varied the scaling of the random component of motion [*s* in Eq. (1)], which is the ratio of mean to random advection in low, medium, and high signal-to-noise scenarios. For our simulations, the total amplitude of the low, medium, and high cases was 5.1, 2.2, and 0.7 km day^{-1}, respectively.

Process noise [$\mathbf{Q}$ in Eq. (6)] is kinematic model uncertainty or unexpected acceleration. For these experiments, $\mathbf{Q}$ is defined by the random component of motion [s in Eq. (1)] and was set accordingly. These experiments test the relative response of the tracking filters to the random component of motion; the schemes nudging tracked floats to follow satellite linear interpolation, fH^{-1} contours, and geostrophic streamlines distort these results and are turned off for all particle runs.

The first observational variable considered is the availability of satellite positioning. Satellite positioning was varied from 0% to 100% of the days each particle was tracked (Fig. 6) for the three signal-to-noise cases considered. As expected, mean trajectory error decreases with increased satellite positioning frequency for all filters. The mean error of the Kalman smoother outperformed the mean error of the Kalman filter and the least squares filter for all satellite positioning and signal-to-noise cases considered. We also find that the relative performance of the Kalman smoother decreased as particle advection signal-to-noise decreased. These results agree with our hypothesis that the decreased signal-to-noise of the float advection will decrease the skill of the kinematics used in the forecast step of the Kalman smoother and Kalman filter. Consequently, their relative performance will approach that of the least squares filter.

Particle tracks were estimated with a range of acoustic noise to test the sensitivity of the filters to TOA uncertainty. TOA uncertainty is included in our calculation as observation noise [$\mathbf{R}$ in the Kalman gain of the forecast update step of Eq. (11)]. TOA uncertainty was varied between 0 and 50 s for all three signal-to-noise cases considered. Mean trajectory error increased with increased simulated TOA uncertainty. The mean error produced by the Kalman smoother outperforms the mean error produced by the Kalman filter and least squares for all values of TOA uncertainty and random float advection considered (Fig. 7). Linear fits of aggregated position errors show that the Kalman smoother not only outperforms the other filters at all three signal-to-noise levels but that the Kalman smoother's performance increases with increasingly noisy TOA observations. However, the least squares solution was insensitive to the signal-to-noise ratios. As the signal-to-noise decreased, this outperformance of the Kalman smoother relative to the least squares filter also decreased.

Finally, we considered the number of acoustic sources heard (Fig. 8). Increasing the number of sound sources heard increases the length of $\mathbf{y}_i^o$ in Eq. (10) and, if unbiased, should improve tracking. Mean trajectory error decreased with increasing numbers of acoustic sources, and the mean trajectory error of the Kalman smoother was lower than both the Kalman filter and the least squares filter. The relative mean trajectory error of the Kalman smoother compared to the Kalman filter also decreased with increasing sound sources heard. This means that the relative performance increase of the Kalman smoother is most pronounced when the most positioning information is available. Mean trajectory error was inversely proportional to the number of sound sources heard for the Kalman filter and Kalman smoother, but initially increased for the least squares filter. This may be due to the fundamental ambiguity of tracking with less than three sources, or because the least squares filter has no forecast, its solutions can easily fall victim to noisy TOA data.

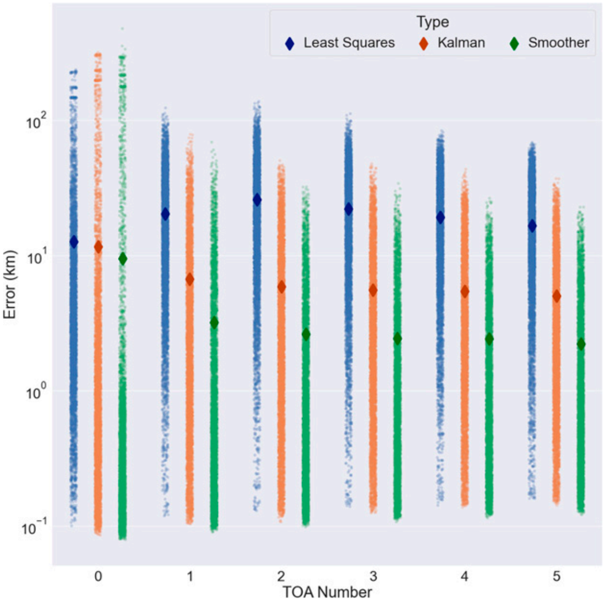

FIG. 8. Trajectory error for numerical simulation for Kalman smoother (green diamond), Kalman filter (orange diamond), and least squares (blue diamond) algorithm for varying quantity of acoustic positioning. Large solid diamonds represent the mean value of each distribution.

b. *DIMES intercomparison*

After our synthetic experiment, we apply the Kalman smoother to real float data, calibrate our filter to optimal cost, and compare our trajectories to ARTOA-derived tracks. DIMES float trajectories were reconstructed with the Kalman smoother and compared with the previously calculated ARTOA trajectories (Balwada et al. 2016) following the preprocessing conventions described in section 4d. As in the DIMES ARTOA tracking, a sound speed of 1.5 km s^{-1} was used in all calculations.

The output of the Kalman smoother depends on prescribed errors and uncertainties; to assess these sensitivities we conducted a tuning experiment to find the ideal combination of data misfit and model size [Eq. (16)]. The optimal parameters for the DIMES experiment as defined in section 4e are 4.5 km for process position noise (large case), 0.75 km day^{-1} for process velocity noise (extra small case), 1.4×10^{-7} rad m^{-1}s^{-1} for fH^{-1} contour noise (large case), 5.0 m^2 s^{-1} geostrophic streamline noise (extra small case), and 2 s TOA noise (extra small case) (Fig. 9). This parameter configuration places relative importance on following geostrophic streamlines, TOA observations, and the velocity forecast, and relatively less importance on fH^{-1} contours and the position forecast.

We observe that the mean misfits are relatively insensitive to process velocity noise and stream noise and that the misfit distributions are non-Gaussian, underscoring the

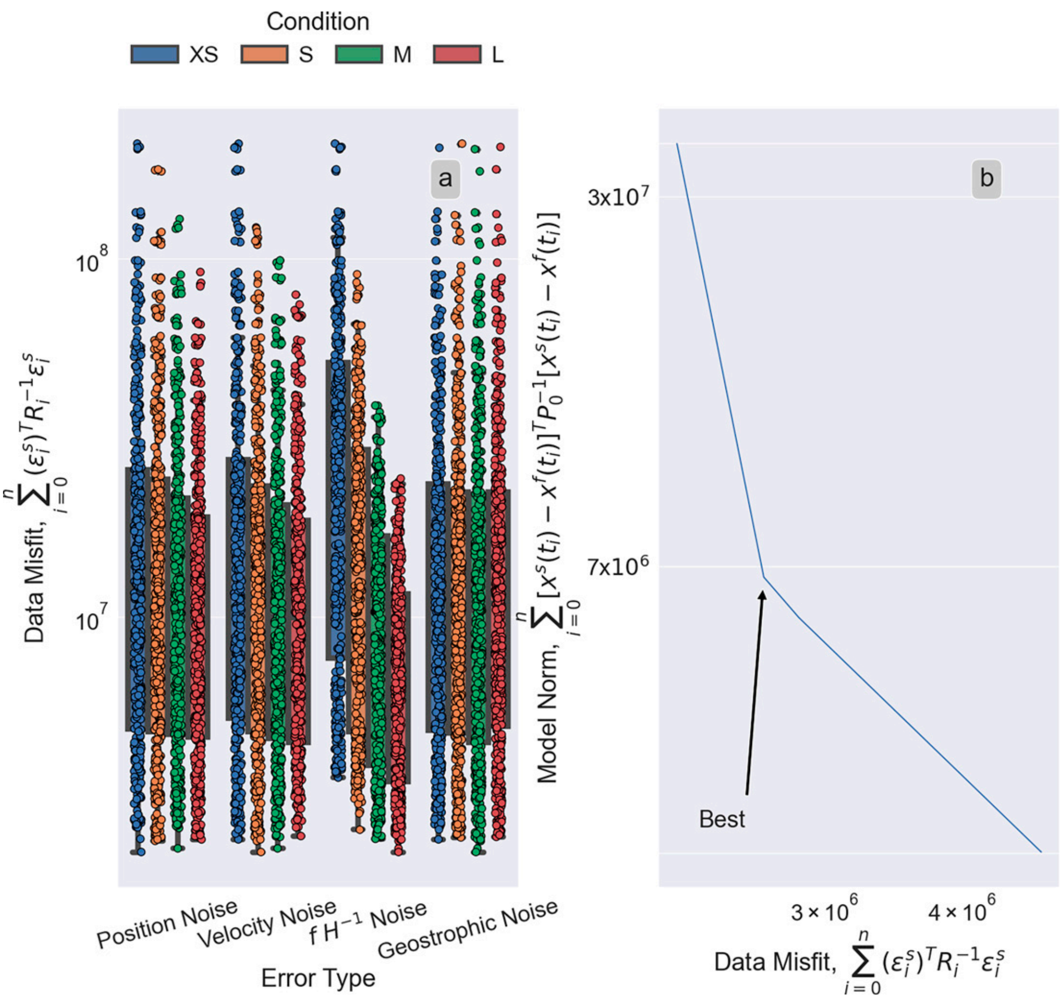

FIG. 9. (a) Sensitivity of DIMES experiment data misfit [Eq. (16)] to changes in position process noise, velocity process noise, fH^{-1} contour noise, and geostrophic streamline noise at extra small (blue), small (orange), medium (green), and large (red) values. (b) Minimum cost overall Weddell Sea tuning runs [J in Eq. (16)] while varying λ from 0 to 100. Curvature minimum of J is identified as the optimal parameter configuration.

importance of properly tuning the filter to the data. Mean misfit appears primarily sensitive to fH^{-1} contour noise. The Hero and Shackleton fracture zones run roughly perpendicular to the Antarctic Circumpolar Current in this region, and this may reduce the skill of fH^{-1} contour-following algorithms.

A fundamental difficulty of reproducing the DIMES trajectories with any filter is that the problem is underconstrained. Over three-quarters of the available ranging data has fewer than the 3 sound sources necessary for an unambiguous fix. This means that two or more solutions can be equally consistent with the available ranging data and yet have substantial differences in trajectories. Figure 10 shows several example trajectories highlighting the similarities and differences between the Kalman smoother and ARTOA trajectories. We observe small differences in well-tracked floats (Fig. 10a), but the general structure is consistent, and the positioning error is relatively low. Underconstrained trajectories (Figs. 10b–d) may have brief periods of close agreement but then diverge for long periods. This divergence can also be seen in the increase of TOA misfit as a function of days since the last acoustic source was heard (Fig. 11). The aggregate of the acoustic record also shows a decrease in mean misfit as a function of the total percentage of the trajectory where the float was acoustically positioned (Fig. 12). The ARTOA to Kalman smoother trajectory difference increased an average of 3.8 km day^{-1} for periods without acoustic ranging.

The ARTOA float tracks achieved lower TOA misfit than the Kalman smoother tracks (Fig. 13a). Unsurprisingly, the ARTOA least squares algorithm produces a solution that is more consistent with available ranging data; our algorithm imposes additional dynamics on the acoustic ranging. Therefore the Kalman smoother trajectories will, in general, have greater misfit. However, because of potential errors in the acoustic ranging, the hypothesis is that those dynamics may help the Kalman smoother have overall better performance at reproducing

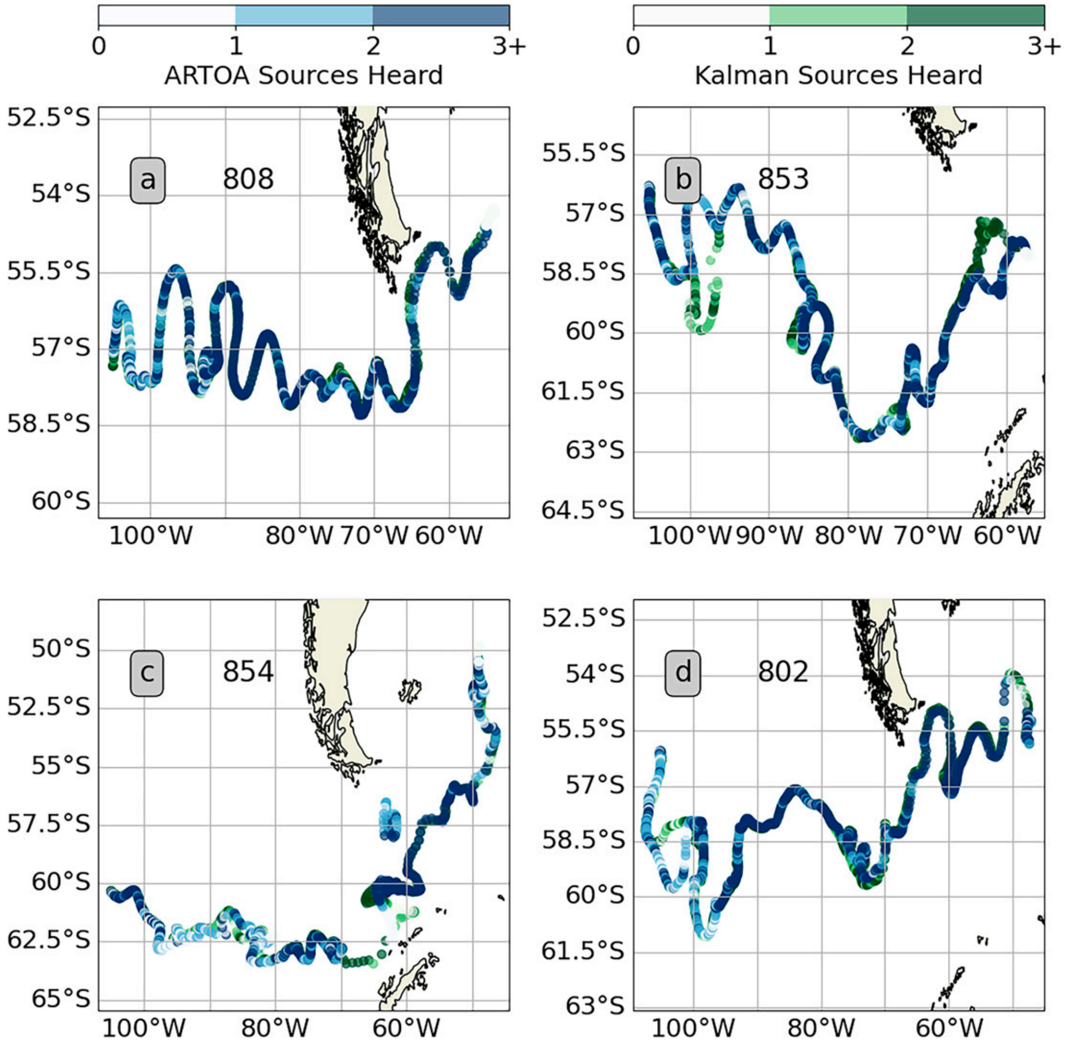

FIG. 10. Comparison of Kalman smoother (green) and ARTOA (blue) trajectories for DIMES floats (a) 808, (b) 853, (c) 854, (d) 802. Float 808 represents a well-tracked float with relatively little difference between Kalman smoother and ARTOA trajectories. Floats 853, 854, and 802 highlight some of the divergences that happen when the solution is not fully constrained.

the true trajectory (as shown in section 5a). Because our algorithm imposes limits on velocity and position change, it may take many additional time steps for the algorithm's solution to converge to an error tolerance within the mean and standard deviation of the experiment. The least squares solutions can reposition its trajectory without bound to achieve maximum consistency with available data. The mean TOA misfit for the ARTOA solution was −0.3 ± 13.1 s, whereas the mean TOA misfit for the Kalman smoother trajectories was −4.1 ± 35.9 s.

The TOA error as a function of sound sources heard is also considered (Fig. 14): a hypothesis for explaining the difference between the ARTOA tracks and our algorithm's tracks has been that the solution becomes unconstrained without regular positioning and, one might assume, that an increased number of sound sources would decrease TOA misfit. These results are more subtle than that line of thinking. We observe the distribution of the TOA misfit between the 20th and 80th percentiles to be between 1.0 and 7.1 s for one sound source, increasing to between 2.5 and 7.6 s for two sound sources, then increasing to a maximum between 4.4 and 12.2 s for three or more sources. A float trajectory can be consistent with one or two lines of position regardless of the uncertainty in the ranging data. However, it can only be consistent with three or more lines of position if the ranging data have no bias or uncertainty. Perfect data, unfortunately, do not occur in the ocean, and all the sources of timing error (sound source clocks, float clocks, speed of sound estimates) may be responsible for this increase in TOA error. The ARTOA to Kalman smoother trajectory difference decreased an average of 13.4 km for each additional sound source heard.

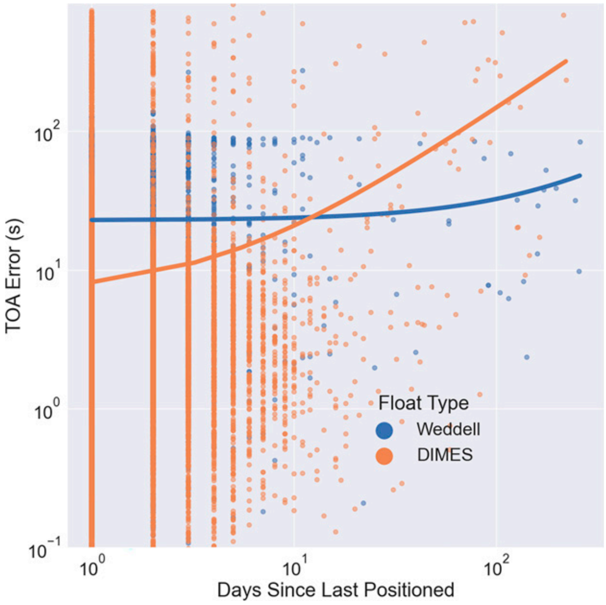

FIG. 11. TOA error for Kalman smoother tracking of the DIMES experiment (orange circle), and Weddell Sea dataset (blue circle) by days since last positioned. Solid lines represent the mean of each distribution.

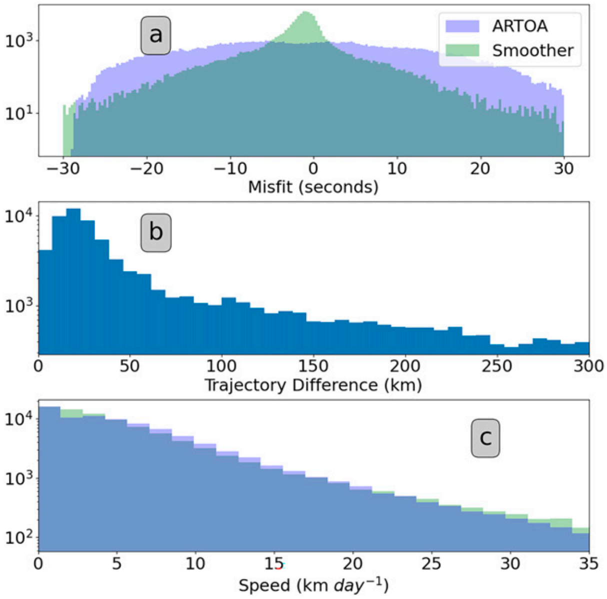

FIG. 13. (a) Histogram of misfit of trajectory with available acoustic ranging for ARTOA (blue) and Kalman smoother (green). (b) Histogram of trajectory difference between Kalman smoother and ARTOA trajectories. (c) Speed histogram for ARTOA trajectories (blue) and Kalman smoother trajectories (green).

Despite these challenges, ARTOA and Kalman smoother trajectories showed many similarities (Fig. 13). The histogram of the trajectory difference between the Kalman smoother trajectories and the ARTOA trajectories peaks at 15.4 km with a mean of 157.9 km and a median value of 44.4 km. A comparison of the Kalman smoother and ARTOA speeds shows a similar distribution, with a higher Kalman smoother velocity peak and a fat tail in the faster end of the distribution

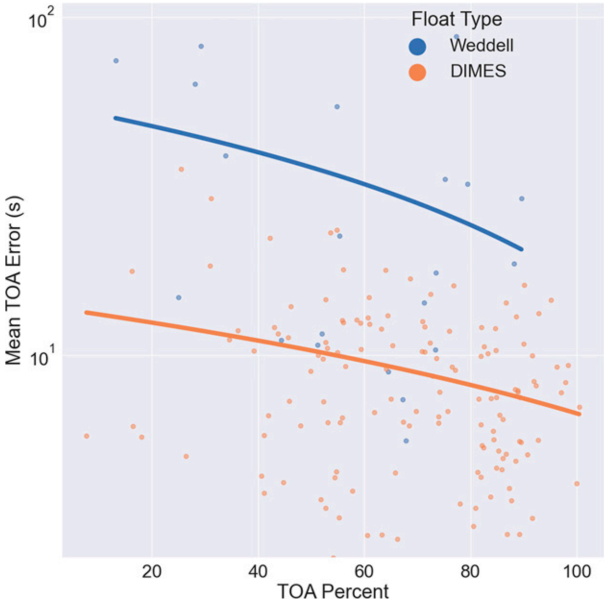

FIG. 12. Mean TOA error for Kalman smoother tracking of the DIMES experiment (orange circle) and Weddell Sea dataset (blue circle) by percentage of trajectory which was acoustically tracked. Solid lines represent the mean of each distribution.

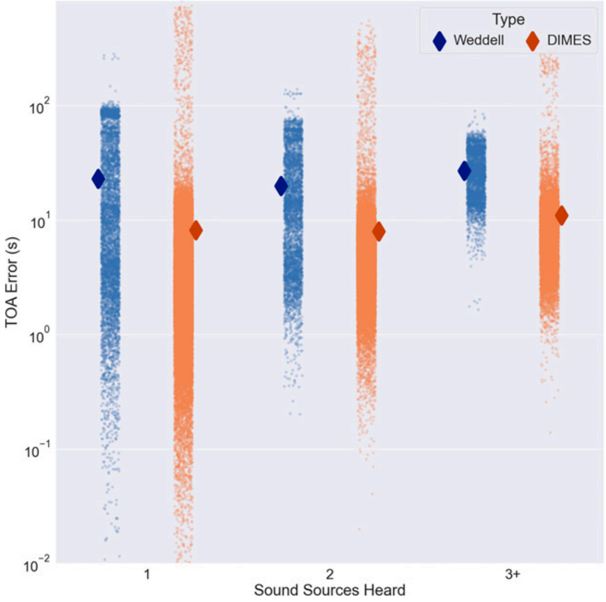

FIG. 14. TOA error for Kalman smoother tracking of the DIMES experiment (orange diamond) and Weddell Sea dataset (blue diamond) for the number of discrete sound sources heard. Large solid diamonds represent the mean value of each distribution.

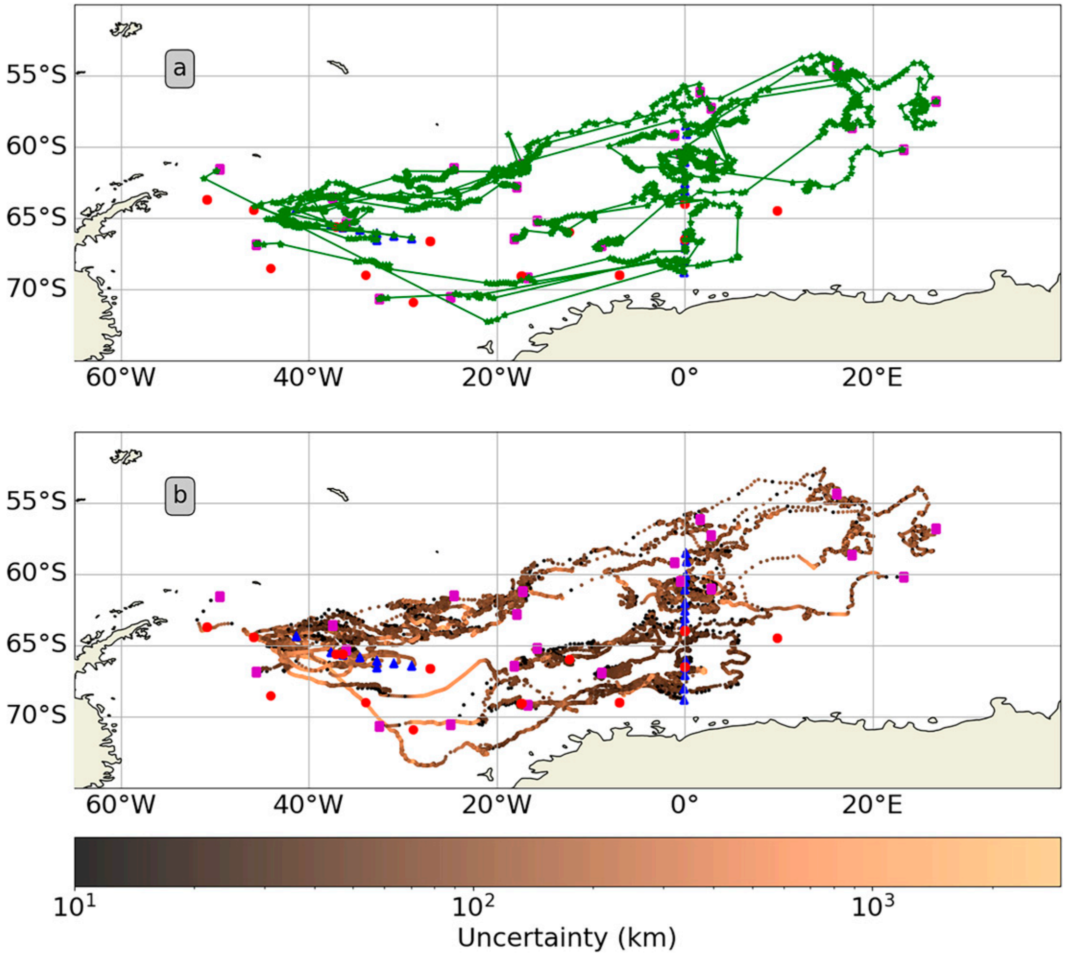

FIG. 15. Trajectories of 22 previously untracked Weddell Sea RAFOS-enabled Argo floats. Red dots represent an array of 13 sound sources. Blue triangles and magenta squares represent the first and last known positions, respectively. (a) Green stars and lines represent GPS positions and satellite linear interpolations as provided by the Argo Global Data Assembly Center, which does not include acoustic tracking. (b) Kalman smoother estimate of true trajectories. Track line colors represent position uncertainty.

(Fig. 13c). The ARTOA float speed pdf peaks at 1.4 km day^{-1} with a mean and median of 6.9 and 4.9 km day^{-1}, respectively. The Kalman smoother pdf speed also peaks at 1.4 km day^{-1} with a mean and median of 7.5 and 4.3 km day^{-1}.

c. *Weddell Sea floats*

Having validated our method with both the numerical experiment and the DIMES float trajectories, we focus on the set of previously untracked floats in the Weddell Sea (Figs. 15 and 16).

Similar to the DIMES intercomparison, the sensitivities of the trajectory solutions were assessed to prescribed parameter uncertainties. Intermittent satellite positioning is available in the Weddell Sea dataset, so we also considered satellite linear interpolation's prescribed uncertainty. The optimal parameter configuration for the Weddell Sea experiment (Fig. 16) as explained in section 4 are 4 s TOA uncertainty (small case), 4.5 km for process position noise (large case), 0.75 km day^{-1} for process velocity noise (extra small case), 0.6 × 10^{-7} rad m^{-1} s^{-1} for fH^{-1} contour noise (extra small case), 30.0 m^2 s^{-1} streamfunction noise (large case). TOA misfit was found to be insensitive to satellite linear interpolation noise at any reasonable values and was set to 120 km. This parameter configuration puts relative importance on the velocity forecast, TOA observations, and the tendency to follow fH^{-1} contours. We observe that data misfit is primarily sensitive to process position noise.

Weddell Sea float trajectories and associated position uncertainties are estimated for the first time (Fig. 15). TOA misfits for the Weddell Sea dataset are generally higher than those for the DIMES dataset (Figs. 11, 12, 14). However, the mean Weddell Sea TOA error is much less after long periods without positioning. This could imply that the data quality of the Weddell Sea experiment is worse than that of DIMES but that the skill of the nudging schemes (particularly fH^{-1} contours) is greater. This implication is reasonable because the

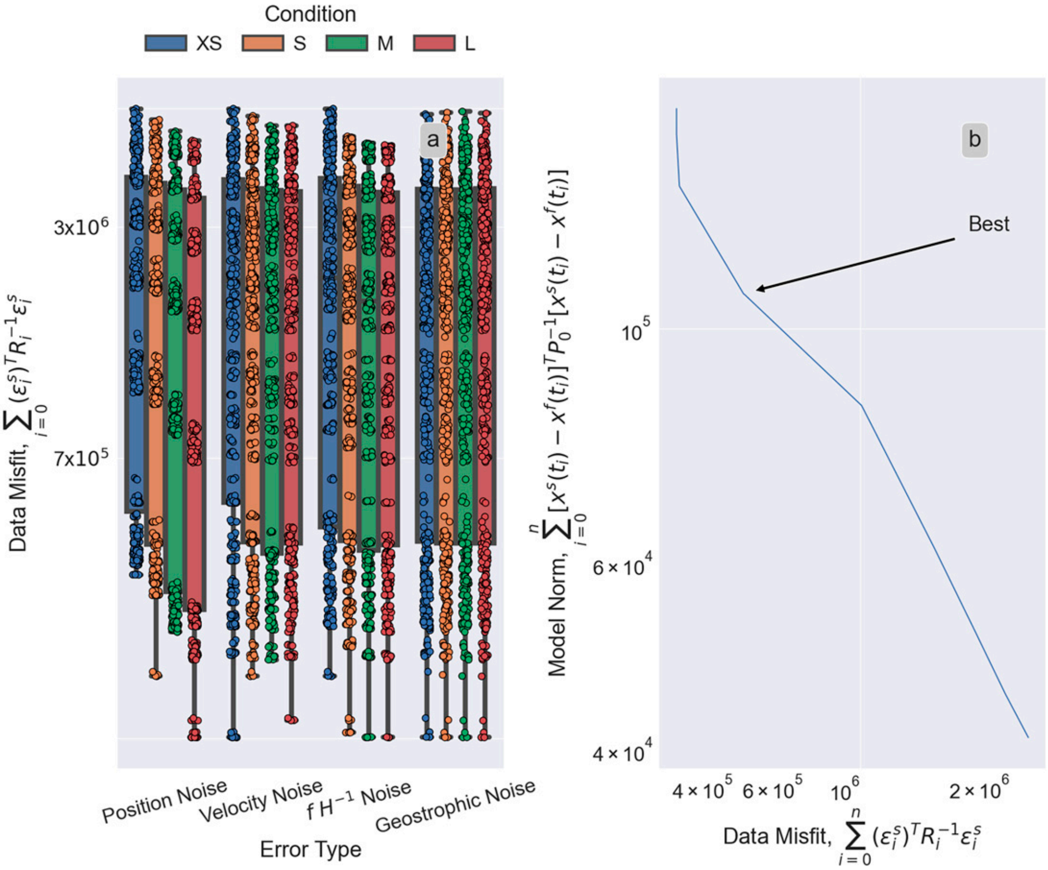

FIG. 16. (a) Sensitivity of Weddell Sea experiment data misfit [Eq. (16)] to changes in position process noise, velocity process noise, fH^{-1} contour noise, and geostrophic streamline noise at extra small (blue), small (orange), medium (green), and large (red) values. (b) Minimum cost overall Weddell Sea tuning runs [J in Eq. (16)] while varying λ from 0 to 100. Curvature minimum of J is identified as the optimal parameter configuration.

Weddell Sea is relatively quiescent compared to Drake Passage and likely has dynamics that are easier to model. Contrary to the DIMES floats, the mean Weddell Sea TOA error continually increases while the standard deviation of TOA error continually decreases (Fig. 14): we observe the distribution of TOA misfit between the 20th and 80th percentiles to be between 2.9 and 43.8 s for one sound source, changing to between 3.8 and 35.0 s for two sound sources, finally increasing to between 15.1 and 39.6 s for three or more sources.

Overall, TOA misfit was higher, and speed was slower than those calculated for DIMES. Similar to the DIMES data (Fig. 17), the residuals are non-Gaussian. Weddell Sea TOA misfit had more bias but less standard deviation compared to the DIMES Kalman smoother trajectories. The mean TOA misfit for the ensemble of reconstructed trajectories was -9.0 ± 14.4 s. While dynamical differences such as the magnitude of mean currents and eddy activity exist between the DIMES experiment and the Weddell Sea, the primary difference between the Weddell Sea and DIMES datasets is that Weddell Sea floats received intermittent satellite positioning, while the DIMES floats did not. The intermittent satellite positioning not only provides a powerful constraint on the trajectory solutions but also helps to calibrate sound source clock drift and moderate the potential nonlinearities associated with sound source misidentification. It is difficult to quantify these effects, but they may be less than the displacement due to the vertically integrated ocean shear that neutrally buoyant floats that drift at depth for long periods have sought to avoid. The speed histogram (Fig. 17b) shows a mean float speed of 5.4 km day^{-1} and a median float speed of 2.1 km day^{-1}.

6. Discussion

Our implementation of the Kalman smoother offers theoretical and operational benefits over the standard least squares solutions. This formulation of Kalman smoothing is designed to be added to updates of float tracking software packages. Checking sound source identification was also an important step in successfully localizing floats in the underice Weddell Sea.

The Kalman smoother is not without weaknesses. Long periods of position loss can cause the filter to produce unphysical estimates that cross onto land or travel against known circulation

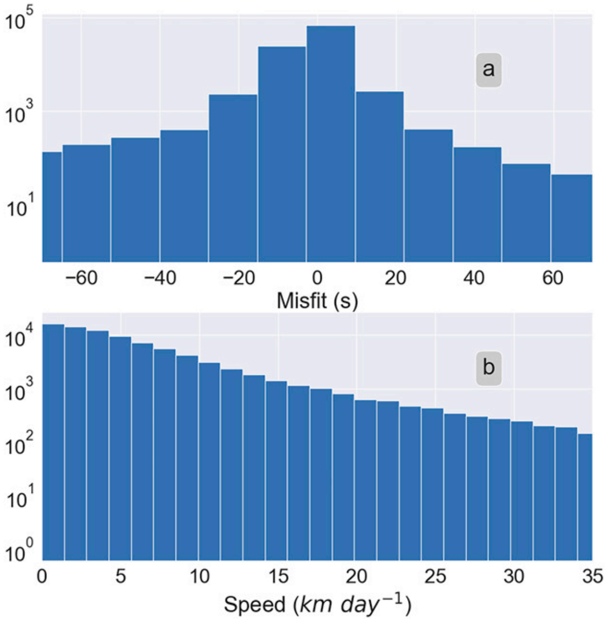

FIG. 17. (a) Histogram of TOA misfit of reconstructed Weddell Sea trajectories with available acoustic ranging. (b) Histogram of calculated Weddell Sea trajectory speeds.

features. The acceptable time of position loss will depend on many factors, including the uncertainty of positioning, sound source configuration, the complexity of the float motion, available satellite positioning, and the tendency of the float to follow geostrophic streamlines. In our analysis, we have found the purely acoustic position estimates of the Kalman smoother after 60 days of position loss to be dubious.

The optimal DIMES and Weddell Sea trajectory solutions have parameter configurations of position noise, velocity noise, and dynamical constraints that imply the Kalman smoother has skill. The ARTOA least squares solution can be approximated by prescribing enormous process noise and nudging scheme noise such that the filter only regards acoustic ranging; this was not the result of the sensitivity experiments. The calculated optimal noise for each dataset emphasizes inputs from specific nudging schemes and the forecast. The low geostrophic streamline noise of the DIMES tuning experiment and the fH^{-1} contour noise of the Weddell Sea tuning experiment highlight the need to include multiple nudging inputs. We have found adding these physical constraints to be important in producing trajectories in the direction of known circulation features with reasonable velocities. It is encouraging that the ideal Weddell Sea float trajectory solution was more strongly affected by the depth-following constraint. At the same time, the geostrophic streamlines were less helpful, as Gray and Riser (2014) note the high uncertainty in their Weddell Sea streamlines due to the very sparse Argo data at the time of their analysis. Satellite linear interpolation was also important in producing reasonable trajectories, although the data misfit was observed to be insensitive to the scaling of 120 km presented in Chamberlain et al. (2018).

7. Conclusions

We have demonstrated a method that combines acoustic ranging, satellite observations, and geostrophic dynamics to constrain float tracks. Our Kalman smoother method includes constraints to follow fH^{-1} contours, geostrophic streamlines, or satellite linear interpolation (when available), and it limits maximum uncertainty in velocity and maximum allowed position change. We have shown that this method is a possible improvement over least squares in an ensemble of numerical simulations and real-world float tracking experiments with degraded acoustic signals.

We validated the Kalman smoother using previous DIMES experiment acoustic ranging data and ARTOA float tracks. We found the trajectories produced by the Kalman smoother to be consistent with available ranging data. We also validated the Kalman smoother using a numerical experiment in which we released and tracked 30 000 artificial particles using simulated acoustic ranging and satellite positioning. Our numerical experiment found that the Kalman smoother was more consistent with the true particle trajectories than the Kalman filter or the least squares solution.

Finally, we applied the Kalman smoother to a previously untracked set of floats in the Weddell Sea. Weddell Sea float tracks and acoustic ranging errors are within standard ranging uncertainties and have been made available publicly through the NOAA Subsurface Float Data Assembly Center. Our dynamical model, which assumes floats follow a combination of fH^{-1} contours, geostrophic streamlines, and satellite linear interpolation, is still somewhat simple. Subsequent software versions that consider known circulation features or sea surface height observations may lead to improvements.

A version of Kalman filtering could be incorporated in future software to identify sound sources; for example, while identifying sources, forecast predictions could be generated from previous sound source selections that inform the user of statistically improbable source choices. In general, clock drift introduced substantial challenges in trajectory reconstruction because of the ocean's relatively high speed of sound. Additionally, although sound sources are identified manually by careful and skilled practitioners, and the Kalman smoother can quantify the statistical probability of a sound source, mistakes in identification are possible—particularly after a long period of ranging loss. Sound source misidentification is a fundamental nonlinearity in this calculation that we do not address. Other methods (Li et al. 2015) or insonification strategies that uniquely identify sound sources have been advanced and could be considered in future deployments (Duda et al. 2006).

This study has focused on the Southern Ocean, but under-ice Argo tracking is also of interest in the Arctic Ocean. Further tests are needed to determine the applicability of the Kalman smoother with our chosen regularizations in the Arctic Ocean.

Acknowledgments. This work was supported by the SOCCOM project under NSF Award PLR-1425989 and by GO-BGC under NSF OCE-1946578. BC was supported by NOAA Grant NA18OAR4310403. We thank 4 anonymous reviewers for their helpful suggestions and remarks, Dr. Olaf Boebel for his dedication to and advancement of acoustic tracking, and Dr. Mathias Morzfeld for insightful conversations and recommendations. KS and CH received support from NSF OCE-1658479.

Data availability statement. ETOPO1 Bathymetric data are available at https://www.ngdc.noaa.gov/mgg/global/. Absolute geostrophic streamlines are available at https://alisonrgray.com/agva/. Weddell Sea subsurface float trajectories have been uploaded to the NOAA Subsurface Float Data Assembly Center available at https://www.aoml.noaa.gov/phod/float_traj/data.php. The latest Kalman smoother code is available at https://github.com/Chamberpain/KalmanSmoother.

REFERENCES

Abrahamsen, E. P., 2014: Sustaining observations in the polar oceans. *Philos. Trans. Roy. Soc.*, **A372**, 20130337, https://doi.org/10.1098/rsta.2013.0337.

Amante, C., and B. Eakins, 2009: ETOPO1 1 arc-minute global relief model: Procedures, data sources and analysis. NOAA Tech. Memo. NESDIS NGDC-24, 25 pp., https://www.ngdc.noaa.gov/mgg/global/relief/ETOPO1/docs/ETOPO1.pdf.

Argo, 2019: Argo float data and metadata from Global Data Assembly Centre (Argo GDAC): Snapshot of Argo GDAC of 8 October 2019. SEANOE, https://doi.org/10.17882/42182#67548.

Balwada, D., K. G. Speer, J. H. LaCasce, W. B. Owens, J. Marshall, and R. Ferrari, 2016: Circulation and stirring in the southeast Pacific Ocean and the Scotia Sea sectors of the Antarctic Circumpolar Current. *J. Phys. Oceanogr.*, **46**, 2005–2027, https://doi.org/10.1175/JPO-D-15-0207.1.

——, J. H. LaCasce, K. G. Speer, and R. Ferrari, 2021: Relative dispersion in the Antarctic Circumpolar Current. *J. Phys. Oceanogr.*, **51**, 553–574, https://doi.org/10.1175/JPO-D-19-0243.1.

Boebel, O., C. Schmid, and W. Zenk, 1997: Flow and recirculation of Antarctic Intermediate Water across the Rio Grande rise. *J. Geophys. Res.*, **102**, 20 967–20 986, https://doi.org/10.1029/97JC00977.

Campbell, E. C., E. A. Wilson, G. W. K. Moore, S. C. Riser, C. E. Brayton, M. R. Mazloff, and L. D. Talley, 2019: Antarctic offshore polynyas linked to Southern Hemisphere climate anomalies. *Nature*, **570**, 319–325, https://doi.org/10.1038/s41586-019-1294-0.

Chamberlain, P. M., L. D. Talley, M. R. Mazloff, S. C. Riser, K. Speer, A. R. Gray, and A. Schwartzman, 2018: Observing the ice-covered Weddell Gyre with profiling floats: Position uncertainties and correlation statistics. *J. Geophys. Res. Oceans*, **123**, 8383–8410, https://doi.org/10.1029/2017JC012990.

Duda, T. F., A. K. Morozov, B. M. Howe, M. G. Brown, K. Speer, P. Lazarevich, P. F. Worcester, and B. D. Cornuelle, 2006: Evaluation of a long-range joint acoustic navigation/thermometry system. *OCEANS 2006*, Boston, MA, IEEE, https://doi.org/10.1109/OCEANS.2006.306999.

Fahrbach, E., M. Hoppema, G. Rohardt, O. Boebel, O. Klatt, and A. Wisotzki, 2011: Warming of deep and abyssal water masses along the Greenwich meridian on decadal time scales: The Weddell Gyre as a heat buffer. *Deep-Sea Res. II*, **58**, 2509–2523, https://doi.org/10.1016/j.dsr2.2011.06.007.

Gille, S. T., K. Speer, J. R. Ledwell, and A. C. Naveira Garabato, 2007: Mixing and stirring in the Southern Ocean. *Eos, Trans. Amer. Geophys. Union*, **88**, 382–383, https://doi.org/10.1029/2007EO390002.

Gould, W. J., 2005: From swallow floats to Argo—The development of neutrally buoyant floats. *Deep-Sea Res. II*, **52**, 529–543, https://doi.org/10.1016/j.dsr2.2004.12.005.

Gray, A. R., and S. C. Riser, 2014: A global analysis of Sverdrup balance using absolute geostrophic velocities from Argo. *J. Phys. Oceanogr.*, **44**, 1213–1229, https://doi.org/10.1175/JPO-D-12-0206.1.

——, and Coauthors, 2018: Autonomous biogeochemical floats detect significant carbon dioxide outgassing in the high-latitude Southern Ocean. *Geophys. Res. Lett.*, **45**, 9049–9057, https://doi.org/10.1029/2018GL078013.

Hogg, N. G., and W. B. Owens, 1999: Direct measurement of the deep circulation within the Brazil Basin. *Deep-Sea Res. II*, **46**, 335–353, https://doi.org/10.1016/S0967-0645(98)00097-6.

Ide, K., P. Courtier, M. Ghil, and A. C. Lorenc, 1997: Unified notation for data assimilation: Operational, sequential and variational (gtspecial issueltdata assimilation in meteorology and oceanography: Theory and practice). *J. Meteor. Soc. Japan*, **75**, 181–189, https://doi.org/10.2151/jmsj1965.75.1B_181.

Jahan, A., K. L. Edwards, and M. Bahraminasab, 2016: *Multi-Criteria Decision Analysis for Supporting the Selection of Engineering Materials in Product Design*. 2nd ed. Butterworth-Heinemann, 252 pp.

Johnson, G. C., and Coauthors, 2022: Argo—Two decades: Global oceanography, revolutionized. *Annu. Rev. Mar. Sci.*, **14**, 379–403, https://doi.org/10.1146/annurev-marine-022521-102008.

Johnson, K. S., and H. Claustre, 2016: Bringing biogeochemistry into the Argo age. *Eos*, **97**, https://doi.org/10.1029/2016EO062427.

Katsumata, K., and H. Yoshinari, 2010: Uncertainties in global mapping of Argo drift data at the parking level. *J. Oceanogr.*, **66**, 553–569, https://doi.org/10.1007/s10872-010-0046-4.

Kimball, P., and S. Rock, 2011: Sonar-based iceberg-relative navigation for autonomous underwater vehicles. *Deep-Sea Res. II*, **58**, 1301–1310, https://doi.org/10.1016/j.dsr2.2010.11.005.

Klatt, O., O. Boebel, and E. Fahrbach, 2007: A profiling float's sense of ice. *J. Atmos. Oceanic Technol.*, **24**, 1301–1308, https://doi.org/10.1175/JTECH2026.1.

LaCasce, J. H., 2000: Floats and *f*/*H*. *J. Mar. Res.*, **58**, 61–95, https://doi.org/10.1357/002224000321511205.

——, R. Ferrari, J. Marshall, R. Tulloch, D. Balwada, and K. Speer, 2014: Float-derived isopycnal diffusivities in the DIMES experiment. *J. Phys. Oceanogr.*, **44**, 764–780, https://doi.org/10.1175/JPO-D-13-0175.1.

Li, T., H. Pareek, P. Ravikumar, D. Balwada, and K. Speer, 2015: Tracking with ranked signals. *Conf. on Uncertainty in Artificial Intelligence* (*UAI*), Amsterdam, Netherlands, AUAI, 474–483, http://auai.org/uai2015/proceedings/papers/12.pdf.

Nguyen, A. T., P. Heimbach, V. V. Garg, V. Ocaña, C. Lee, and L. Rainville, 2020: Impact of synthetic arctic Argo-type floats in a coupled ocean–sea ice state estimation framework. *J. Atmos. Oceanic Technol.*, **37**, 1477–1495, https://doi.org/10.1175/JTECH-D-19-0159.1.

Ollitrault, M., and A. Colin de Verdière, 2014: The ocean general circulation near 1000-m depth. *J. Phys. Oceanogr.*, **44**, 384–409, https://doi.org/10.1175/JPO-D-13-030.1.

Parker, R. L., 1994: *Geophysical Inverse Theory*. Vol. 1. Princeton University Press, 386 pp., https://doi.org/10.1515/9780691206837.

Ramsey, A. L., H. H. Furey, and A. S. Bower, 2018: Deep floats reveal complex ocean circulation patterns. *Eos*, **99**, https://doi.org/10.1029/2018EO105549.

Rauch, H. E., F. Tung, and C. T. Striebel, 1965: Maximum likelihood estimates of linear dynamic systems. *AIAA J.*, **3**, 1445–1450, https://doi.org/10.2514/3.3166.

Reeve, K. A., O. Boebel, T. Kanzow, V. Strass, G. Rohardt, and E. Fahrbach, 2016: A gridded data set of upper-ocean hydrographic properties in the Weddell Gyre obtained by objective mapping of Argo float measurements. *Earth Syst. Sci. Data*, **8**, 15–40, https://doi.org/10.5194/essd-8-15-2016.

Riser, S. C., and Coauthors, 2016: Fifteen years of ocean observations with the global Argo array. *Nat. Climate Change*, **6**, 145–153, https://doi.org/10.1038/nclimate2872.

Roemmich, D., and Coauthors, 2019: On the future of Argo: A global, full-depth, multi-disciplinary array. *Front. Mar. Sci.*, **6**, 439, https://doi.org/10.3389/fmars.2019.00439.

Rossby, T., D. Dorson, and J. Fontaine, 1986: The RAFOS system. *J. Atmos. Oceanic Technol.*, **3**, 672–679, https://doi.org/10.1175/1520-0426(1986)003<0672:TRS>2.0.CO;2.

Sarmiento, J. L., N. Gruber, M. A. Brzezinski, and J. P. Dunne, 2004: High-latitude controls of thermocline nutrients and low latitude biological productivity. *Nature*, **427**, 56–60, https://doi.org/10.1038/nature02127.

Spiesecke, S., 2018: Analysis and modelling of RAFOS signal propagation under the Antarctic sea-ice for positioning Argo floats. M.S. thesis, Dept. of Electronics Engineering, Alfred Wegener Institute, 78 pp.

Swallow, J. C., 1955: A neutral-buoyancy float for measuring deep currents. *Deep-Sea Res.*, **3**, 74–81, https://doi.org/10.1016/0146-6313(55)90037-X.

Wallace, L. O., E. M. Van Wijk, S. R. Rintoul, and B. Hally, 2020: Bathymetry-constrained navigation of Argo floats under sea ice on the Antarctic continental shelf. *Geophys. Res. Lett.*, **47**, e2020GL087019, https://doi.org/10.1029/2020GL087019.

Webster, S. E., L. E. Freitag, C. M. Lee, and J. I. Gobat, 2015: Towards real-time under-ice acoustic navigation at mesoscale ranges. *Proc. 2015 IEEE Int. Conf. on Robotics and Automation*, Seattle, WA, IEEE, 537–544, https://doi.org/10.1109/ICRA.2015.7139231.

WHOI, 2017: ARTOA. Accessed 9 December 2017, https://www2.whoi.edu/site/bower-lab/rafosfloats-soundsources/artoa-float-tracking-software/.

Wong, A. P. S., and S. C. Riser, 2011: Profiling float observations of the upper ocean under sea ice off the Wilkes Land coast of Antarctica. *J. Phys. Oceanogr.*, **41**, 1102–1115, https://doi.org/10.1175/2011JPO4516.1.

Wooding, C. M., H. H. Furey, and M. A. Pachece, 2005: RAFOS float processing at the Woods Hole Oceanographic Institution. WHOI Tech. Rep. WHOI-2005-02, 43 pp., https://darchive.mblwhoilibrary.org/bitstream/handle/1912/55/WHOI-2005-02.pdf?sequence=1&isAllowed=y.

Wunsch, C., 2006: *Discrete Inverse and State Estimation Problems: With Geophysical Fluid Applications*. Cambridge University Press, 396 pp. https://doi.org/10.1017/CBO9780511535949.

Yamazaki, K., S. Aoki, K. Shimada, T. Kobayashi, and Y. Kitade, 2020: Structure of the subpolar gyre in the Australian-Antarctic basin derived from Argo floats. *J. Geophys. Res. Oceans*, **125**, e2019JC015406, https://doi.org/10.1029/2019JC015406.